

# The Impacts of Midlevel Moisture on the Structure, Evolution, and Precipitation of Afternoon Thunderstorms: A Real-Case Modeling Study at Taipei on 14 June 2015

JYONG-EN MIAO<sup>a,b</sup> AND MING-JEN YANG<sup>b</sup>

<sup>a</sup> *Air Navigation and Weather Services, Civil Aeronautics Administration, Taipei, Taiwan*

<sup>b</sup> *Department of Atmospheric Sciences, National Taiwan University, Taipei, Taiwan*

(Manuscript received 29 September 2021, in final form 28 March 2022)

**ABSTRACT:** A severe afternoon thunderstorm (ATS) system developed within the Taipei basin on 14 June 2015, which produced intense rainfall (with a rainfall rate of  $131 \text{ mm h}^{-1}$ ) and urban-scale flooding. A control simulation (CNTL) using the Weather Research and Forecasting (WRF) Model with the horizontal grid size nested down to 500 m was performed to capture reasonably well the onset of the sea breeze, the merger of convective cells, and the evolution of the afternoon thunderstorm system. Four numerical sensitivity experiments with the increase or decrease of midlevel (700–500 hPa) relative humidity (RH) of 10% and 20% were conducted, and simulation results were compared with those from the CNTL. Although the response of convection to midlevel RH was somewhat nonlinear, sensitivity experiments showed that a dry layer at middle levels would result in stronger cold pool, more intense convection, stronger updraft, more graupel particles, stronger net latent heating above the melting level, and a much larger area of the potential flooding region [ $>40 \text{ mm (30 min)}^{-1}$ ]. The estimation of bulk entrainment rate provided evidence that the entrainment rate could be reduced by stronger cold pool and the widening of moist convection area. Three terrain-removal sensitivity experiments indicated that Taipei basin modulated the response of convection intensity to midlevel RH. The basin terrain confined the outflow associated with ATS and forced it to converge with the moist sea breeze continuously, providing a favorable dynamic and thermodynamic environment for subsequent convection development. This “basin confinement effect” may be crucial for short-duration rainfall extremes over complex terrain.

**SIGNIFICANCE STATEMENT:** This study has examined the impact of midlevel moisture on the structure, evolution, and precipitation of an afternoon thunderstorm system that produced intense rainfall at Taipei using eight numerical experiments based on high-resolution model outputs. Our findings explain how a drier layer at middle levels would produce a more intense thunderstorm system, although the response of convection intensity to midlevel moisture is somewhat nonlinear. In addition, it is found that terrain could modulate the response of convection to midlevel moisture, which is rarely discussed in previous studies.

**KEYWORDS:** Thunderstorms; Moisture/moisture budget; Cloud resolving models; Cold pools; Entrainment; Trajectories; Rainfall

## 1. Introduction

Taipei basin (TB), the largest population and economic center in Taiwan, is strongly influenced by afternoon thunderstorms (ATSS) during the summer season (Chen et al. 2007). Thunderstorms can produce severe weather phenomena such as severe turbulence, low-level wind shear, low ceilings and visibilities, hail, and lightning, which are hazardous to aviation safety and human activity. Moreover, during the summer season, severe ATSS and their associated flash floods frequently cause severe property damage and traffic hazards over the Taipei metropolitan area. Although ATSS have significant economic impacts, it is still a challenging forecast issue for the weather forecasters due to our limited knowledge of their physical mechanisms.

Radar reflectivity climatology showed that thunderstorms in northern Taiwan often occur during 1500–1600 LST (Lin et al. 2011). When sea breeze collides with thunderstorm outflows near foothills south of TB, it can enhance lifting at the collision boundary. Therefore, ATSS are most active along

the windward slopes of the mountains in Taiwan rather than at mountain peaks (Johnson and Breach 1991; Jou 1994; Chen et al. 2001; Chen et al. 2007).

In Jou et al. (2016), observational characteristics of urban flash flood in TB associated with the ATS on 14 June 2015 were documented. They found that urban flooding associated with ATS was closely related to the merger of convective cells. The merger of convective cells produced an enlarged precipitation area and stronger radar echoes extending to much higher altitudes. Enhanced horizontal convergence produced by the sea-breeze circulation and cold-air outflow from earlier developed storms was favorable for cell merger. (Jou et al. 2016; Miao and Yang 2018).

Using the high-resolution Weather Research and Forecasting (WRF) Model simulation with the horizontal grid size nested down to 0.5 km, Miao and Yang (2020, MY20 hereafter) investigated this severe ATS event. It was found that convection at the mountain peak (foothill) was initiated by the upslope wind (sea breeze). The convective cells at the mountain slope merged into the severe thunderstorm complex associated with the deep cold pool, which was higher than the level of free convection (LFC) for the air parcels within the

Corresponding author: Ming-Jen Yang, mingjen@as.ntu.edu.tw

DOI: 10.1175/JAS-D-21-0257.1

© 2022 American Meteorological Society. For information regarding reuse of this content and general copyright information, consult the [AMS Copyright Policy](#) ([www.ametsoc.org/PUBSReuseLicenses](#)).

sea breeze. When the moist parcels within sea breeze were lifted up to the LFC at the leading edge of cold pool, conditional instability could be released effectively, leading to subsequent development of the ATS system. Numerical sensitivity experiments indicated that cloud microphysics and coastal terrain also exerted considerable influences on the rainfall intensity for this ATS system.

However, besides low-level moisture brought by the sea breeze, Banchiao sounding at the TB for this ATS event also had deep dry air at middle levels (see Fig. 1c in MY20), which seemed to contradict the ATS occurrence checklist found in previous studies (Lin et al. 2012; Chen et al. 2016, C16 hereafter). It seems probable that the dry layer at middle levels would produce stronger evaporative cooling and cold pool, greater convergence at gust-front head, stronger convection, and more intense precipitation over the TB. Surprisingly, the sensitivity of ATS evolution and precipitation characteristics to the ambient midlevel moisture is not examined in previous studies on ATSs, which is the main theme of this study.

Although some studies have investigated the influences of midlevel dry air on convection development in the past, the detailed physical mechanisms remain underexplored. Many previous studies indicated that dry midlevel air is conducive to the formation of strong downdrafts (Fawbush and Miller 1954; Foster 1958; Browning and Ludlum 1962; Johns and Doswell 1992). Yang and Houze (1995) found that when the environmental moisture was reduced by half, the mesoscale downdraft was 22% stronger and the squall-line orientation became more upright. Gilmore and Wicker (1998) investigated the response of supercell morphology to the midtropospheric dryness. They found that supercells forming in environments with moderate vertical wind shear, large instability, and very dry midtropospheric air produced strong low-level outflow. James and Markowski (2010, hereafter JM10) found that dry air above the cloud base reduced the intensity of the quasi-linear convective systems and supercells, as measured by updraft mass flux and total condensation and rainfall. Moreover, the impact of dry air was highly sensitive to the environmental CAPE, with the deleterious effects of dry air on convection intensity being much lesser at higher CAPE. For tropical oceanic convection, the existence of environmental dry air above cloud base is considered to be detrimental to convection intensity (Brown and Zhang 1997; Parsons et al. 2000). Takemi et al. (2004) found that moisture profiles at mid- to upper levels had a strong impact on the vertical development of tropical cumulus clouds. The midtropospheric moist layer was favorable for the development of cumulus congestus and cumulonimbus. These studies mostly used an idealized simulation to study convection in a horizontally homogeneous environment (i.e., a single thermodynamic profile). However, environmental heterogeneities can certainly influence convective systems (Richardson et al. 2007). Therefore, a real-case modeling study which represents these heterogeneities in the environment is still needed, especially for the complex terrain near the TB.

Following our previous research (Miao and Yang 2018; MY20) on this ATS system over the TB on 14 June 2015, a series of numerical simulations with the WRF Model are

conducted in this study to investigate the impacts of midlevel moisture content on the convection structure, storm evolution, and precipitation intensity. The first objective is to understand the physical processes leading to the intense ATS when a midlevel layer of dry air occurs. One control experiment and four sensitivity experiments using different environmental midlevel relative-humidity profiles are performed. The second objective is to examine how Taiwan terrain modulates the response of ATS to the midlevel moisture content. Three midlevel-moisture sensitivity experiments are conducted with Taiwan terrain totally removed. The synoptic environment and the ATS occurrence for this severe thunderstorm case are described in section 2. Section 3 describes the model configuration and experimental design. The main results are presented in section 4. The response of ATS to midlevel moisture in the absence of Taiwan terrain is discussed in section 5. Discussion and summary are given in section 6.

## 2. ATS occurrence criteria revisited

Figure 1 displays the synoptic environment for the ATS system over the TB at 0000 UTC 14 June 2015. It is clear from Fig. 1a that the southerly wind prevailed over Taiwan ahead of a distant surface front, indicating that the synoptic forcing was weak. Southwesterly flow at the 850-hPa level brought warm and moist air (with  $\theta_e > 340$  K) from the South China Sea to Taiwan (Fig. 1b). On the other hand, the southwesterly wind prevailed over Taiwan at the 700- and 500-hPa levels (Figs. 1c,d). The ridge associated with the subtropical high pressure system extended over the Bashi Channel and South China Sea (Fig. 1d). Meanwhile, the relative humidity (RH) near Taiwan was 40%–50% at the 700-hPa level and 20%–40% at the 500-hPa level, implying deep dry air at middle levels.

Backward trajectories over 48 h were calculated for northern Taiwan (Fig. 2a) with the internet-based version of the Hybrid Single-Particle Lagrangian Integrated Trajectory model (HYSPPLIT) (Stein et al. 2015; Rolph et al. 2017) using the Global Data Assimilation System (GDAS) dataset with 0.5° latitude–longitude resolution. A total of 36 air parcels started from northern Taiwan, with initial heights of 5000 m MSL. The 48-h duration was selected to consider the synoptic-scale evolution appropriately. Figure 2 indicates that midlevel dry air parcels originated from the Philippine Sea and were transported by the anticyclonic flow at the vicinity of western North Pacific subtropical high.

The synoptic conditions for this case satisfy the criteria for ATS occurrence (C16) except for the dewpoint depressions at surface (5.0 K in this case but 2.1 K in C16) and 500-hPa level (22.0 K in this case but 8.3 K in C16). Lin et al. (2012) also indicated that a moist midlevel environment was favorable for ATS development. However, there was deep midlevel dry air on this day (Figs. 1c,d). The dewpoint depressions at the 700-hPa (10.9 K) and 500-hPa levels (22.0 K) were much larger than those in Lin et al. (2012) (9.5 K at 700 hPa and 11.0 K at 500 hPa). We hypothesize that the midlevel dry air between 700 and 500 hPa may play an important role in the development of this severe ATS event. Therefore, one control and four sensitivity experiments are conducted to explore the

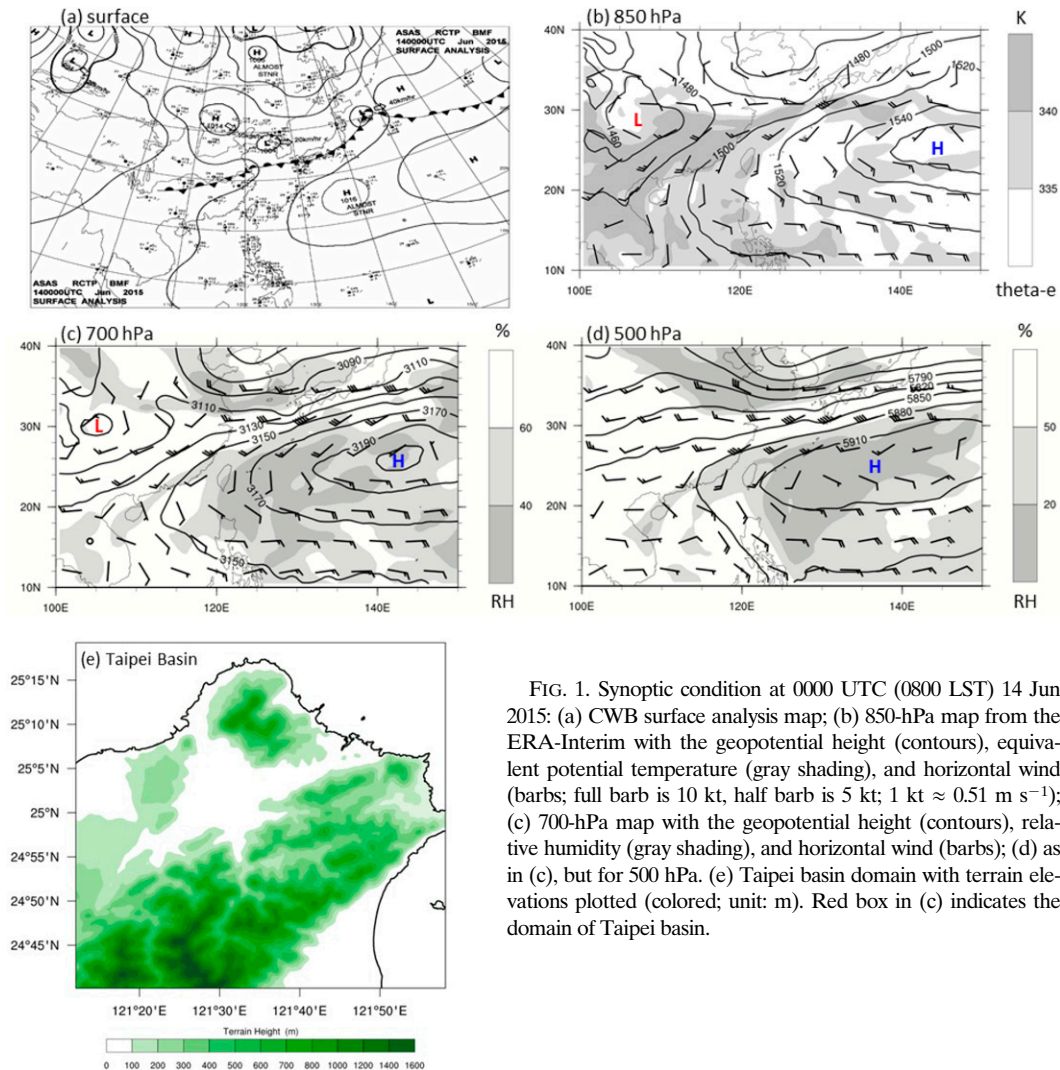


FIG. 1. Synoptic condition at 0000 UTC (0800 LST) 14 Jun 2015: (a) CWB surface analysis map; (b) 850-hPa map from the ERA-Interim with the geopotential height (contours), equivalent potential temperature (gray shading), and horizontal wind (barbs; full barb is 10 kt, half barb is 5 kt; 1 kt  $\approx$  0.51 m s<sup>-1</sup>); (c) 700-hPa map with the geopotential height (contours), relative humidity (gray shading), and horizontal wind (barbs); (d) as in (c), but for 500 hPa. (e) Taipei basin domain with terrain elevations plotted (colored; unit: m). Red box in (c) indicates the domain of Taipei basin.

sensitivity of ATS development to the midlevel RH (see Table 1). Moreover, terrain sensitivity experiments are also conducted to examine the orographic effect.

### 3. Numerical model and experimental design

#### a. WRF configuration

In MY20, the authors used the Advanced Research version of WRF to simulate the severe ATS event at TB on 14 June 2015. The simulation was compared with the surface and radar observations to show that the CNTL simulation can reasonably capture the evolution of sea breeze and ATS system over TB (see Figs. 5, 6, 8 in MY20). The simulated sounding was also compared to the one observed to illustrate that the thermodynamic environment was reproduced reasonably well by the CNTL run (see Fig. 4 in MY20). In this study, we use the same model configuration as MY20 to simulate the evolution of ATS, and the configuration is mentioned briefly here.

The Advanced Research version of the Weather Research and Forecasting Model (WRF-ARW version 3.4.1; Skamarock et al. 2008) is used to simulate this Taipei basin ATS event from 1200 UTC 13 June to 1200 UTC 14 June 2015, with a forecast period of 24 h. Four nested domains with the horizontal grid sizes of 13.5, 4.5, 1.5, and 0.5 km are used, respectively (see Fig. 3 in MY20). Two-way interaction between inner and outer grids is considered. Fifty-five eta ( $\eta$ ) levels are used in the vertical with higher resolution within the planetary boundary layer (eight layers below 1-km height). The model top is at 20 hPa, and the time step for the outermost domain is 5 s. The WRF Model outputs at interval of 5 min are analyzed in this study.

The physical parameterization schemes used in the model include the Kain–Fritsch cumulus parameterization (Kain and Fritsch 1993), the WDM6 microphysics parameterization (Lim and Hong 2010), Rapid Radiative Transfer Model (RRTM) longwave radiation parameterization (Mlawer et al.

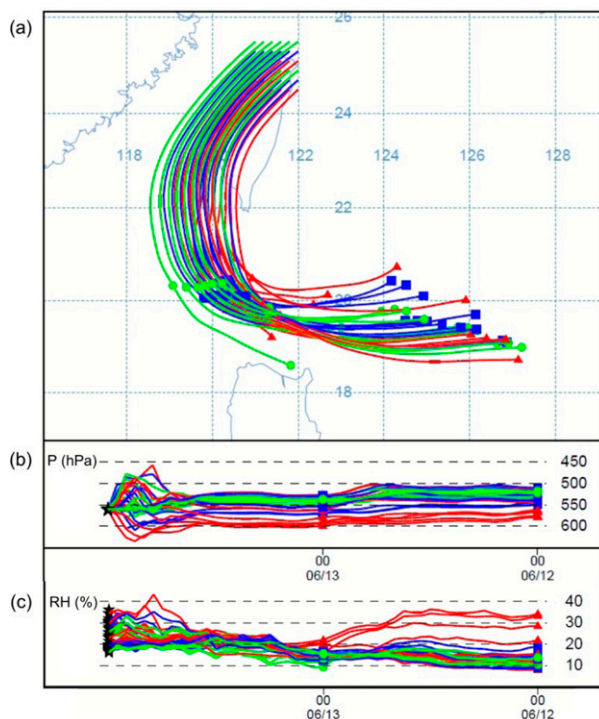


FIG. 2. Backward trajectory analysis (for 48 h): (a) horizontal trajectories; (b) pressure along the trajectories; (c) relative humidity along the trajectories. The starting (ending) time of backward trajectories is 0000 UTC 14 Jun (0000 UTC 12 Jun) 2015. Trajectories were initialized over northern Taiwan ( $24.5^{\circ}$ – $25.5^{\circ}$ N,  $121^{\circ}$ – $122^{\circ}$ E) at 5 km MSL for a total of 36 trajectories.

1997), Dudhia (1989) shortwave parameterization, and the Yonsei University (YSU) planetary boundary layer (PBL) parameterization (Hong and Pan 1996). Note that the cumulus scheme is used only in the outermost domain (with a horizontal grid size of 13.5 km), assuming that the grid sizes of other domains (with the grid sizes of 4.5, 1.5, and 0.5 km, respectively) are able to resolve convection explicitly. The initial and boundary conditions are from the ERA-Interim dataset, updated every 6 h with the latitude–longitude resolution at  $0.75^{\circ}$  (Dee et al. 2011).

### b. Sensitivity experiments on midlevel RH

In addition to the control simulation (CNTL), four numerical experiments are performed to examine the sensitivity of convective structure and evolution to the variations of midlevel RH. Experiments with RH higher (or lower) by 10% and 20% than that of CNTL at middle levels (700–500 hPa) are called the WET10 and WET20 (or DRY10 and DRY20), respectively. We modify the midlevel RH over the entire WRF domain for domains 1–4 (initial condition). The temperature profile is unchanged while the dewpoint is changed over 700–500-hPa levels. Moreover, the RH is also altered in the boundary condition. Note that if the RH is more (less) than 100% (0%) after adjustment, then it remains 100% (0%) to prevent physically

TABLE 1. 700- and 500-hPa dewpoint depressions, 700–500-hPa mean relative humidity, downdraft convective available potential energy (DCAPE) and precipitable water (PW) for the observed and simulated Banchiao sounding at 0800 LST (0000 UTC) 14 Jun 2015 ( $t = 12$  h). DCAPE values are based upon parcels descending from the 600 hPa. The location of Banchiao sounding station is shown in Fig. 2a in MY20.

Expt	500-/700-hPa $T - T_d$ (K)	500–700-hPa mean RH (%)	DCAPE ( $\text{J kg}^{-1}$ )	PW (mm)
OBS	22.0/10.9	27	1518	44.7
DRY20	37.7/12.0	19	1489	41.6
DRY10	27.8/10.4	27	1318	43.6
CNTL	22.9/8.9	35	1166	45.7
WET10	20.4/7.6	41	1046	47.6
WET20	19.0/6.4	46	949	49.4

unrealistic conditions in the moisture field. The rest of the model configurations are the same as those in CNTL.

The initial moisture vertical profiles, along with those 12 h later, are illustrated in Fig. 3. For the initial conditions ( $t = 0$  h; see Fig. 3a), the midlevel water vapor mixing ratio was increased (decreased) by a maximum of about 2.0 (1.5)  $\text{g kg}^{-1}$  in WET20 (DRY20) experiment compared to the CNTL. By  $t = 12$  h (Fig. 3b), the midlevel dewpoint depressions had increased in all experiments, although the magnitude of the initial mixing ratio perturbations was maintained.

Table 1 compares the 500- and 700-hPa dewpoint depressions ( $T - T_d$ ), 700–500-hPa mean RH, downdraft convective available potential energy (DCAPE) and precipitable water (PW) for the Banchiao sounding at  $t = 12$  h. The CNTL simulation reasonably captured the deep dry air at 700–500 hPa. A more detailed comparison of the simulated and observed sounding can be seen in MY20 (see their Fig. 4). Note that the observed sounding shows a decent DCAPE ( $1518 \text{ J kg}^{-1}$ ).

In these experiments, the percent increase in PW relative to the CNTL ranges from 4% in WET10 experiment to 8% in WET20 experiment, and the percent decrease in DCAPE relative to the CNTL ranges from 10% in WET10 experiment to 19% in WET20 experiment. On the other hand, the percent decrease in PW relative to the CNTL ranges from 5% in DRY10 experiment to 9% in DRY20 experiment, and the percent increase in DCAPE relative to the CNTL ranges from 13% in DRY10 experiment to 28% in DRY20 experiment.

MY20 indicated that CAPE at Banchiao station increased by a factor of 4 with abundant moisture transported by the sea breeze from 0800 to 1200 LST (see their Fig. 10), providing large convective instability for the development of the ATS. To examine the environment where the convection developed, we compared some thermodynamic variables at noon (Table 2), about 1 h before the ATS occurred within basin plain. Near-surface temperatures of all experiments are the same except for WET20. WET20 has the lowest near-surface temperature because the 850–800-hPa saturated layer in WET20 reduced solar radiation reaching the land surface. It is clear that CAPE differences between all experiments are quite minor except for WET20. For instance, CAPE in DRY20

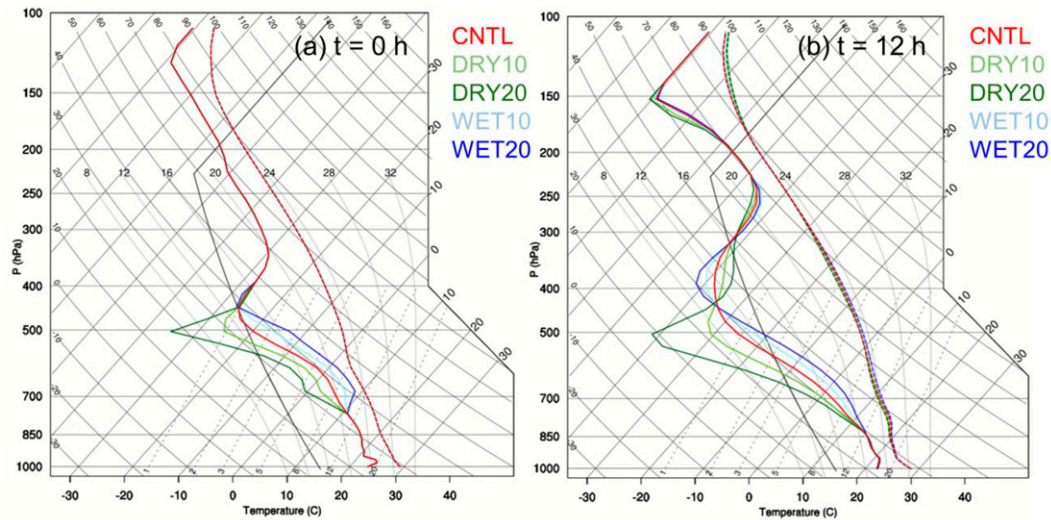


FIG. 3. Simulated soundings of temperature and dewpoint from five experiments at Banchiao station at (a)  $t = 0$  h and (b)  $t = 12$  h.

is only 3% greater than that in CNTL run, and CAPE in WET10 is 2% less than that in CNTL. Note that CAPE in WET20 is 14% less than that in CNTL, mainly due to the lower near-surface temperature in WET20. Thus, perturbing the midlevel moisture has a minor influence on CAPE unless there is a saturated layer.

**4. Results**

*a. Convection evolution and precipitation*

Figure 4 displays the storm evolution in column-maximum radar reflectivity for five experiments. Overall, all experiments showed a similar pattern of three distinct phases in the life cycle of the ATS. The first phase was characterized by the scattered convection over the mountain slope south of TB (Figs. 4a–e). The scattered convection over the southern slope gradually merged into the thunderstorm complex during the second phase (Figs. 4f–j). Afterward, the thunderstorm complex propagated to the central basin and produced intense rainfall in the third phase (Figs. 4k–o). Note that WET20 experiment showed the earliest convection initiation, followed by WET10, CNTL, DRY10, and DRY20 experiments, indicating a monotonic relation between the timing of convection

initiation and midlevel moisture content. However, the ATS was stronger in CNTL, DRY10, and DRY20 experiments (Figs. 4f–j).

Previous studies (Kuang and Bretherton 2006; Khairoutdinov and Randall 2006) indicated that the widening of moist convection area could mitigate the detrimental effect of dry-air entrainment. To measure the convection area of the ATS system more objectively, we define the convection size as the maximum connected area of radar reflectivity and updraft intensity within the TB (see the black box with the size of 60 km × 45 km in Fig. 4a). Figure 5a shows the evolution of convection size in terms of the maximum connected area of column-maximum radar reflectivity greater than 55 dBZ. Overall, the convection size was larger in CNTL, DRY10, and DRY20 experiments, compared to that in WET10 and WET20 experiments, suggesting that the ATS system was wider in drier midlevel environments although DRY10 experiment had a slightly narrower size than CNTL. Figure 5b displays the convection size in terms of upper-level (8 km MSL) updraft velocity greater than 3 m s<sup>-1</sup>. Similarly, the area of upper-level connected updraft was greater in experiments with drier midlevel environments (i.e., the CNTL, DRY10, and DRY20).

Figure 6a illustrates the increase of accumulated rainfall over the TB domain during 1200–1500 LST. WET20 experiment had the most accumulated rainfall; CNTL and WET10 runs featured similar accumulated rainfall; DRY10 and DRY20 had less accumulated rainfall than CNTL. Note that accumulated rainfall in DRY20 surpassed that in DRY10 after 1430 LST, indicating that the relationship between accumulated rainfall and environmental midlevel moisture content was nonlinear. Figure 6b displays the time series of the number of TB-domain grid points ( $N$ ) with rainfall exceeding 40 mm in 30 min (i.e., rainfall intensity greater than 80 mm h<sup>-1</sup>). The drainage standard of the rainwater sewers in Taipei City is 78.8 mm h<sup>-1</sup> (Chen and Liu 2014), indicating that Taipei’s urban

TABLE 2. Temperature and water vapor mixing ratio at 35 m AGL (lowest eta level), CAPE and PW for the simulation experiments at 1205 LST 14 Jun 2015 ( $t = 16.08$  h). Note that CAPE includes the virtual temperature effect.

Expt	$T_0$ (°C)	$q_0$ (g kg <sup>-1</sup> )	CAPE (J kg <sup>-1</sup> )	PW (mm)
DRY20	32.0	17.4	3597	46.7
DRY10	32.0	17.6	3488	49.3
CNTL	32.0	17.6	3480	51.8
WET10	32.0	17.7	3421	54.6
WET20	31.6	17.8	2976	56.5

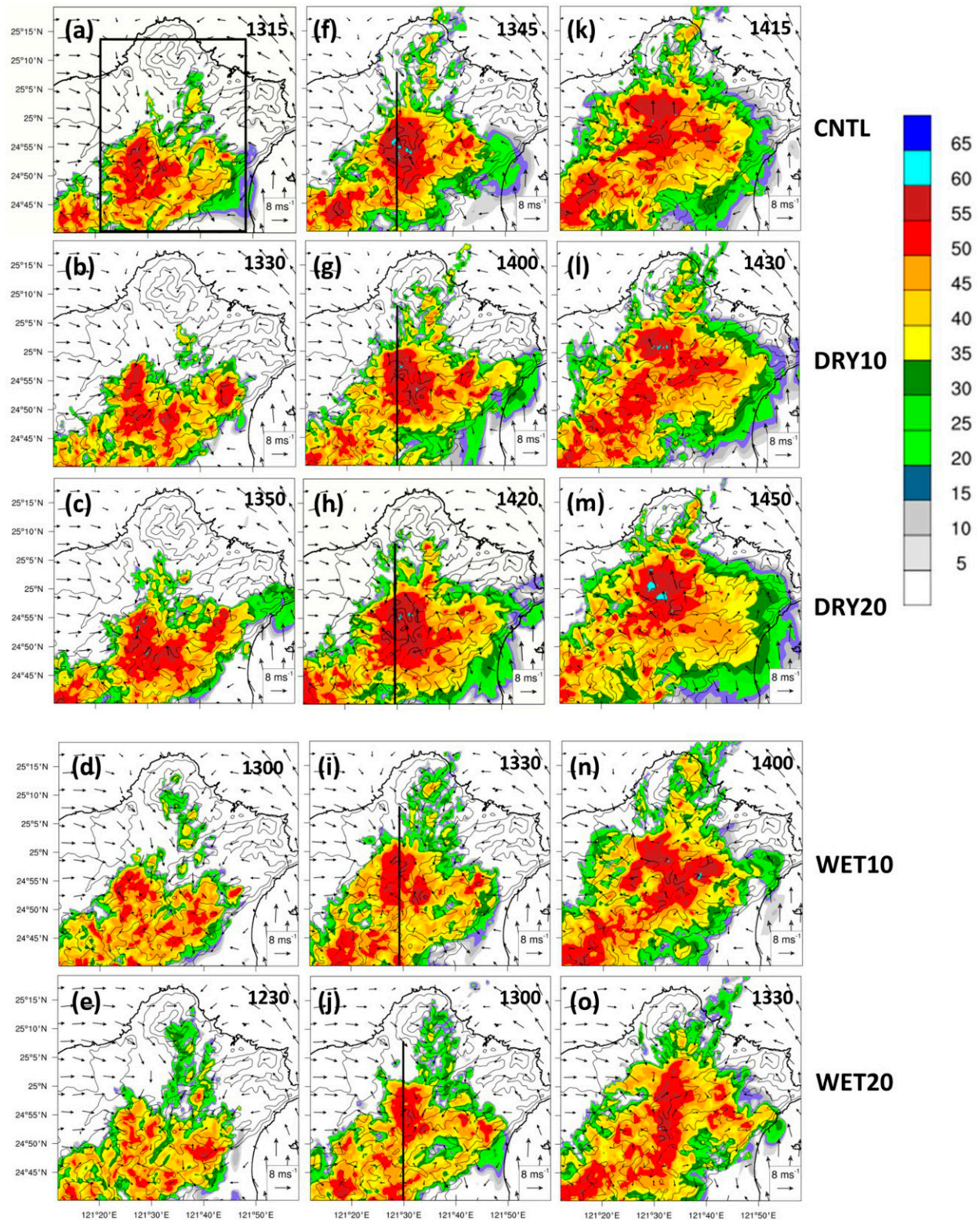


FIG. 4. Simulated column-maximum radar reflectivity fields (unit: dBZ; colored) for the (a),(f),(k) CNTL, (b),(g),(l) DRY10, (c),(h),(m) DRY20, (d),(i),(n) WET10, and (e),(j),(o) WET20 experiments at (a)–(e) phase 1, (f)–(j) phase 2, and (k)–(o) phase 3. See the text for further explanation. The time in LST is indicated at the upper-right corner in each panel. Black box in (a) is the TB domain for the calculations in Figs. 5–10, 15, and 19–21 and Table 3. Black lines in (f)–(j) show the location of the vertical cross sections in Fig. 14.

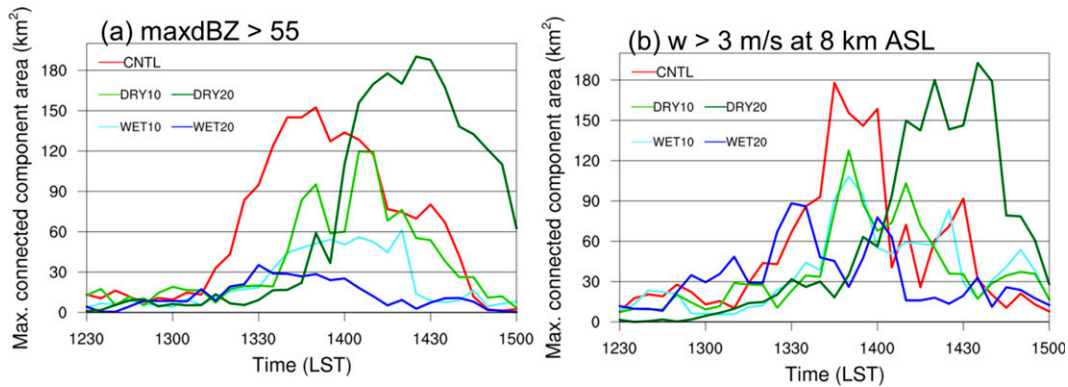


FIG. 5. Time series of TB-domain maximum connected area (unit:  $\text{km}^2$ ) of (a) column-maximum radar reflectivity greater than  $55 \text{ dBZ}$  and (b) vertical velocity greater than  $3 \text{ m s}^{-1}$  at  $8 \text{ km}$  MSL from the CNTL, DRY10, DRY20, WET10, and WET20 experiments. The TB domain is for the rectangular box in Fig. 4a.

flooding will occur if the rainfall intensity surpasses the drainage standard. Therefore, Fig. 6b shows the sequence of potential flooding area (i.e., grid area  $\times N$ ) in Taipei City. Surprisingly, the total area of the potential flooding region during 1200–1500 LST was largest in DRY20 ( $N \approx 200 + 160 = 360$ ), 20% more than that in CNTL ( $N \approx 80 + 220 = 300$ ). DRY10 and WET10 experiments featured similar area of potential flooding region ( $N \approx 55$ ,

82% less than that in CNTL. WET20 run had the least grid points ( $N \approx 15$ ) for flooding potential, about 95% less than that in CNTL run. These results suggest that domain accumulated rainfall was not positively related to flooding potential (or rainfall rate). Furthermore, the occurrence of short-duration intense rainfall produced by the ATS system increased markedly with the decreased midlevel moisture. For instance, the area of region with rainfall intensity greater than  $80 \text{ mm h}^{-1}$  was approximately 95% greater in CNTL than that in the WET20 run, but the PW difference between the CNTL and WET20 was only  $3.7 \text{ mm}$  or 8% (see Table 1).

*b. Evolution of updraft, downdraft, and entrainment rate*

Following JM10, updraft mass flux  $M_u$  and downdraft mass flux  $M_d$  are calculated with the formula, respectively,

$$M_u = \rho A_u W_u,$$

$$M_d = \rho A_d W_d,$$

where  $\rho$  is air density,  $A_u$  ( $A_d$ ) is the area covered by updrafts (downdrafts), and  $W_u$  ( $W_d$ ) is the vertical velocity averaged across all updrafts (downdrafts) in the TB domain. A grid point is defined as an updraft (downdraft) point if the vertical velocity is greater (less) than  $0.5 \text{ m s}^{-1}$  ( $-0.5 \text{ m s}^{-1}$ ) and the sum of the cloud water and cloud ice mixing ratios is greater than  $0.01 \text{ g kg}^{-1}$ . The local maxima of updraft mass flux were located near 4 and 11 km MSL (Fig. 7), respectively. The 4-km maximum was associated with gust-front lifting, while the 11-km maximum was caused by buoyancy-driven ascent. The updraft mass flux was stronger in CNTL and DRY20 experiments, with the maxima near  $10^9 \text{ kg s}^{-1}$ . Moreover, the low-level updraft was stronger in CNTL, DRY10, and DRY20 experiments, compared to those in the WET10 and WET20 runs. On the other hand, DRY10 experiment had weaker upper-level updraft mass flux than that in the CNTL, which might be due to narrower convection size (Fig. 5) and more dilution by entrainment in DRY10 experiment (Fig. 9). Updraft mass flux in WET20 was the weakest among all five simulations.

The downdraft mass flux was stronger in CNTL and DRY20 experiments, with the maximum magnitude of  $10^9 \text{ kg s}^{-1}$  (Fig. 8). These results are consistent with the intense short-

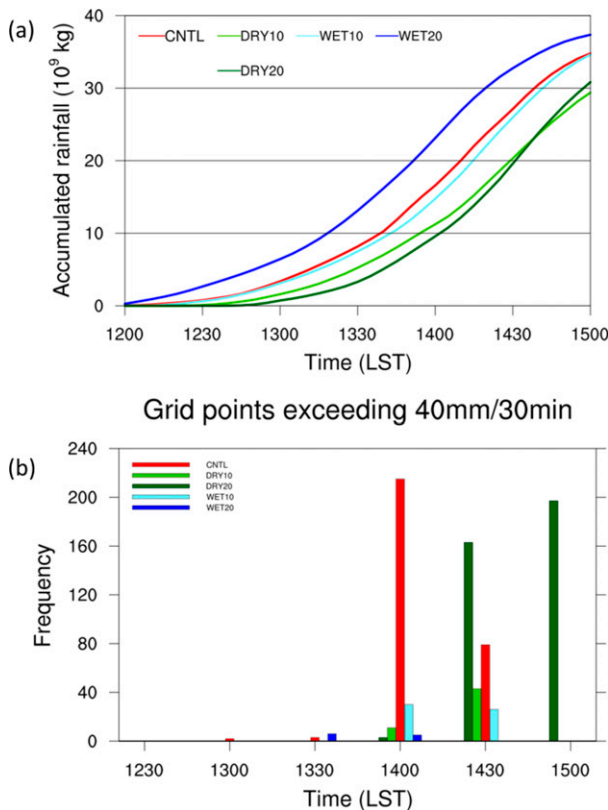


FIG. 6. (a) Time series of TB domain-summed rainfall accumulation (unit:  $10^9 \text{ kg}$ ) for five experiments. (b) Number of TB-domain grid points with 30-min rainfall exceeding  $40 \text{ mm (30 min)}^{-1}$  for five experiments.

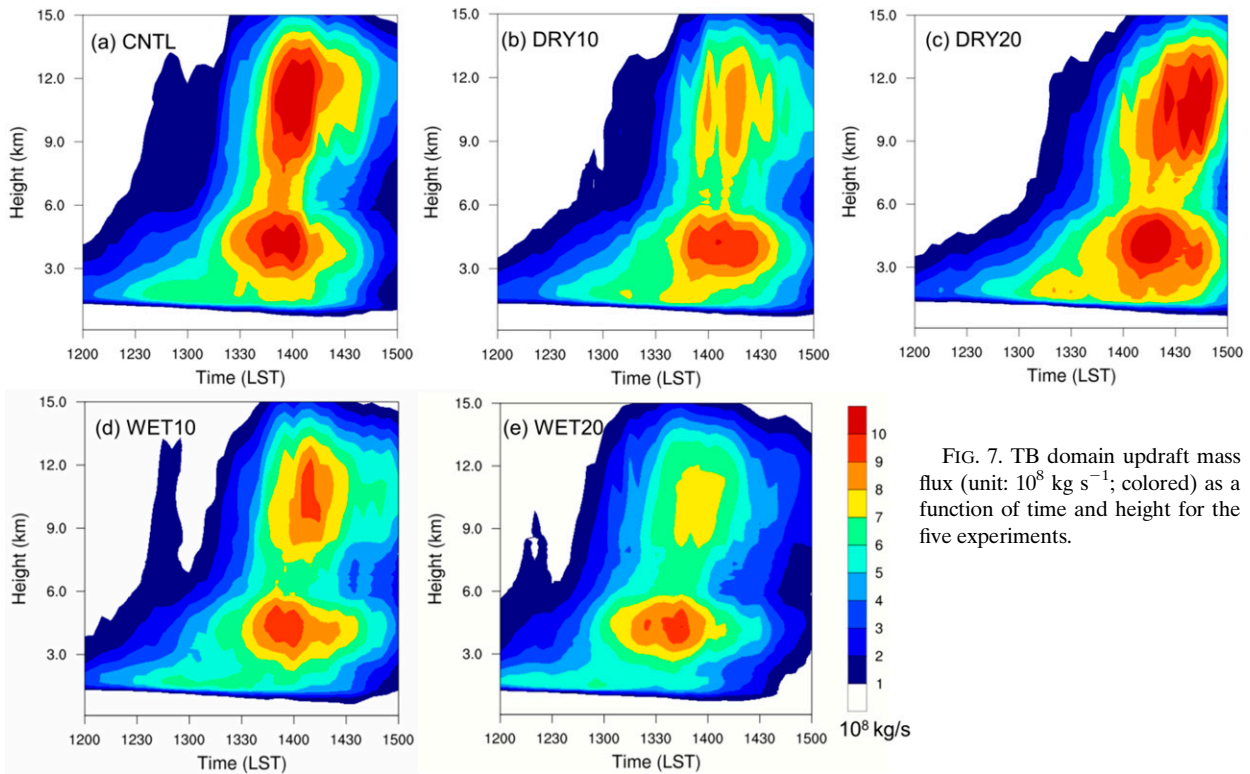


FIG. 7. TB domain updraft mass flux (unit:  $10^8 \text{ kg s}^{-1}$ ; colored) as a function of time and height for the five experiments.

duration rainfall in these experiments (Fig. 6b). On the other hand, the downdraft mass fluxes of the DRY10 and WET10 experiments were comparable, whereas the WET20 downdraft mass flux was the weakest among the five experiments. Compared to CNTL, the maximum magnitude of downdraft mass flux in WET20 was weaker by about 30%. Furthermore, the upper-level (9–15 km MSL) downdraft mass flux in WET20 was significantly weakened because of the reduced updraft mass flux (Fig. 7). Interestingly, WET20 experiment had the most accumulated rainfall within the TB (Fig. 6a) but the weakest downdraft mass flux and rainfall intensity (Fig. 6b). It suggests that the rainfall in WET20 was more spatially and temporarily homogeneous than that in the others.

Following Kurowski et al. (2018), the bulk entrainment rate  $\varepsilon$  is estimated as

$$\varepsilon = \frac{\partial \phi_c}{\partial z} / (\phi_e - \phi_c), \quad (1)$$

where  $\phi$  is moist static energy (MSE), which is approximately conserved during moist adiabatic process. Subscripts  $c$  and  $e$  denote the value within updrafts and environment, respectively. To emphasize the role of intense updrafts, the updraft MSE ( $\phi_c$ ) is calculated as an updraft-mass-flux weighted mean for the updrafts within the TB domain (Hohengger and Bretherton 2011). The environmental MSE ( $\phi_e$ ) is calculated by averaging all nonupdraft grid points within the TB domain.

To elucidate the role of entrainment process, the evolution of TB-domain-mean bulk entrainment rate for all five experiments is shown in Fig. 9. During the period of shallow

convection development (1200–1300 LST in the CNTL, DRY10, and DRY20), the entrainment rate was the largest (with the maximum value of  $6 \times 10^{-4} \text{ m}^{-1}$ ). With the intensification of updraft mass flux (Fig. 7), the entrainment rate was abruptly decreased to approximately  $1 \times 10^{-4} \text{ m}^{-1}$  in CNTL, DRY10, and DRY20 experiments (see the dash ellipses in Fig. 9). The decrease of entrainment rate was associated with the increasing storm size (Fig. 5). In contrast, the entrainment rate did not decrease with the increasing updraft mass flux in WET10 and WET20 experiments. This implies that even in a drier midlevel environment, the entrainment effect could be reduced by wider convection area and thus higher maximum vertical velocity occurred (Fig. 10). Note that the entrainment rate began to increase after the increase of downdraft mass flux (Fig. 8), which might be due to the narrowing of convection area and the updraft–downdraft interaction.

### c. Cold pool and CAPE consumed

Previous research (e.g., Feng et al. 2015; Moseley et al. 2016) has shown that cold-pool dynamics can play a critical role in the transition from shallow to deep convection. Following previous studies (Tompkins 2001; Feng et al. 2015; MY20), buoyancy  $b$  is calculated with the formula

$$b = g \frac{\theta_p - \overline{\theta_p}}{\overline{\theta_p}}, \quad (2)$$

where  $g$  is the gravitational acceleration, and the overbar indicates the domain mean within the TB area. The density potential temperature  $\theta_p$  (Emanuel 1994) is defined as

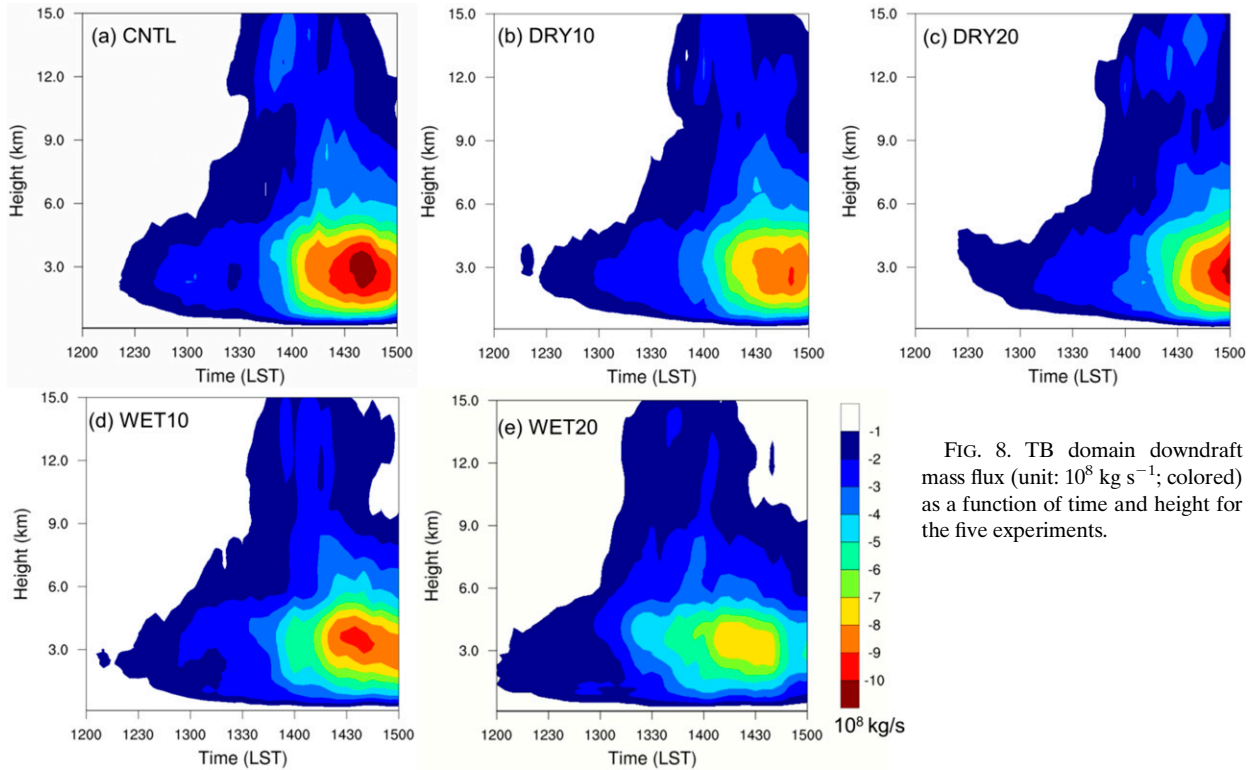


FIG. 8. TB domain downdraft mass flux (unit:  $10^8 \text{ kg s}^{-1}$ ; colored) as a function of time and height for the five experiments.

$$\theta_p = \theta(1 + 0.608q_v - q_l), \tag{3}$$

where  $\theta$  is the potential temperature, and  $q_v$  and  $q_l$  are the mixing ratios of water vapor and condensate (including liquid and ice phases), respectively. Cold-pool propagation speed  $C$  (Rotunno et al. 1988; Bryan and Parker 2010) is defined as

$$C = \sqrt{-2 \int_0^h b \, dz}, \tag{4}$$

where  $b$  is the buoyancy in Eq. (2), and  $h$  is the depth of cold pool which is defined as the height at which  $b$  first exceeds  $-0.05 \text{ m s}^{-2}$ . Note that cold-pool intensity is proportional to its propagation speed  $C$ , as shown in Fig. 11. At first, the cold pools in CNTL, DRY10, and DRY20 were stronger and then merged together. After the cold pools merged, they became much stronger and had a larger connected area with stronger low-level updrafts. In contrast, cold pools in WET10 and WET20 were weaker and more discrete. Feng et al. (2015) suggested that more clouds were triggered at the collision boundary of cold pools, favoring the formation of wider clouds. These wider clouds would reduce the entrainment rate and develop into deep convection in a dry midlevel environment.

Trajectories for air parcels passing through the ATS systems in CNTL, DRY20, and WET20 experiments were used to examine the differences in simulated convective structures. Trajectories were calculated from 5-min model outputs for a total of 200 air parcels originating just north of the gust front

before the ATSS propagated into central TB, with initial heights of 400 and 600 m MSL (Fig. 12). A perturbation of 200 m was added in the starting vertical level of air parcels to increase the trajectory spread. These 30-min forward trajectories were calculated and plotted using the Visualization and Analysis Platform for Atmospheric, Oceanic and Solar Research (VAPOR; Clyne and Rast 2005; Clyne et al. 2007) software. Thirty minutes after the release of the near-surface moist air parcels, most of the moist parcels from sea breeze in CNTL and DRY20 experiments were lifted along the leading edge of the deep cold pool (Fig. 12). A majority of these parcels in these experiments rose above the melting level ( $\sim 5 \text{ km MSL}$ ), with the final heights more than 15 km MSL (Figs. 12c,f). Note that these trajectories had overshooting characteristics. In contrast, only a few parcels in WET20 experiment rose above the shallow cold pool (Fig. 12i), whereas many parcels remained trapped at lower levels. Furthermore, 63% and 91% of air parcels rose above the melting level ( $\sim 5 \text{ km MSL}$ ) in CNTL and DRY20 experiments, respectively (Fig. 13). On the contrary, only 24% of parcels rose above the melting level in WET20 experiment. These results indicate that air parcels within sea-breeze circulation in CNTL and DRY20 runs were “lifted” to much higher levels than those in WET20 run. For this ATS system occurring in an environment with weak synoptic forcing, the percentage of surface-based parcels that rose in deep convection was proportional to the intensity of cold pool.

To shed more light on the effects of cold-pool dynamics, the evolution of thermodynamic instability and cold-pool height

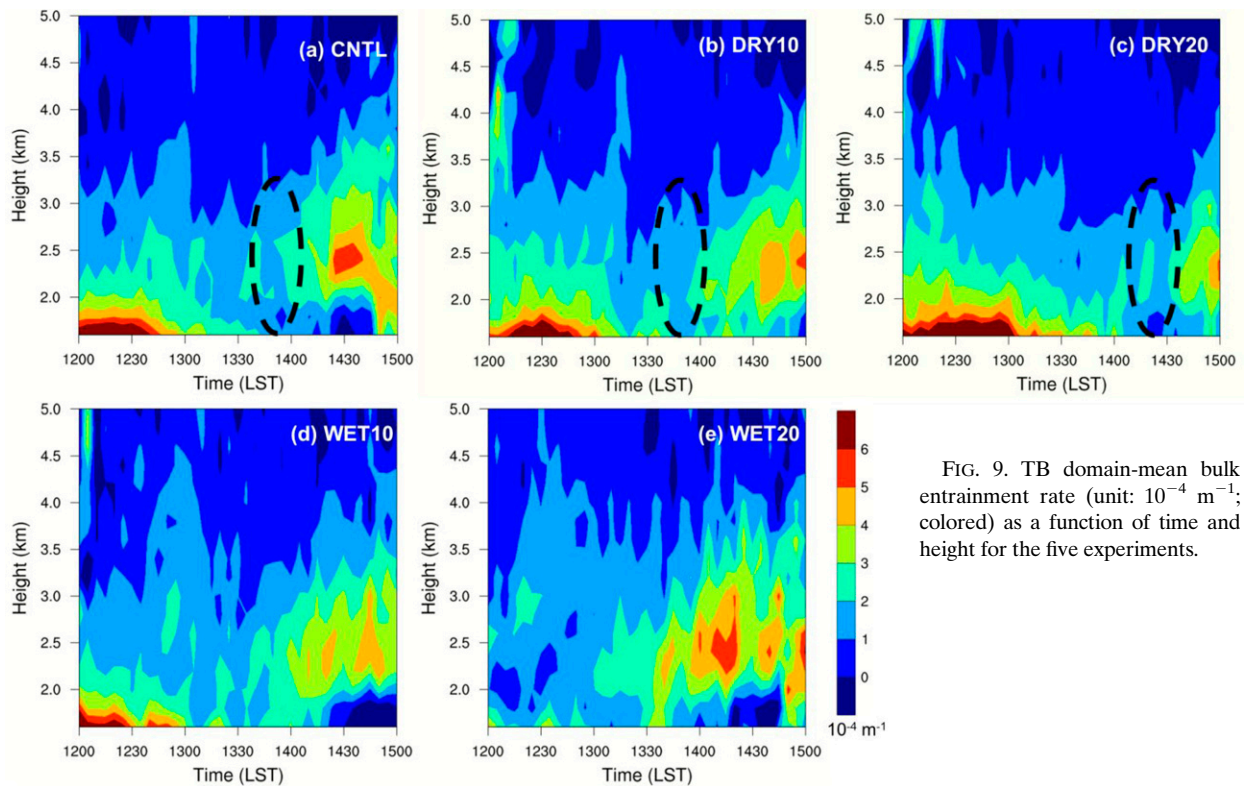


FIG. 9. TB domain-mean bulk entrainment rate (unit:  $10^{-4} \text{ m}^{-1}$ ; colored) as a function of time and height for the five experiments.

before and after the simulated ATS systems propagated into the TB is shown in Fig. 14. Before the cold pool propagated into the TB, CAPEs over central Taipei reached more than  $1500 \text{ J kg}^{-1}$  (Figs. 14a,c,e,g,i) due to solar heating and moisture brought by the sea breeze (MY20). The updraft ( $1 \text{ m s}^{-1}$ ) associated with the gust front extended from surface to 5-km height in CNTL, DRY10, and DRY20 experiments. Afterward, the passage of stronger cold pools in CNTL, DRY10, and DRY20 experiments resulted in a dramatic release of CAPE, as indicated by the CAPE decrease to less than  $500 \text{ J kg}^{-1}$  (Figs. 14b,d,f). In contrast, CAPEs over central Taipei in WET10 and WET20 experiments remained relatively high

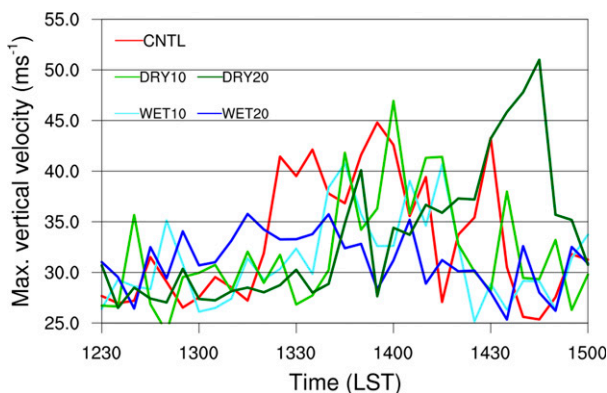


FIG. 10. Time series of TB domain-maximum vertical velocity (unit:  $\text{m s}^{-1}$ ) for the five experiments.

even after the passage of their weaker cold pools (Figs. 14h,j). If the initial midlevel RH in the CNTL increased by 20% (i.e., WET20 experiment), then the cold-pool depth (speed) decreased by 50% (21%), and the CAPE release rate decreased by 81% (Table 3). Figure 15 displays that DRY20 experiment had the most latent heating in the upper level, followed by CNTL, DRY10, WET10, and WET20. These results imply that the cold pools in wetter midlevel environments (i.e., WET10 and WET20) were too weak to lift the moist air parcels within sea breeze. As a result, CAPEs over the TB could not be released effectively.

The simulation results indicate that the response of convection to midlevel RH is somewhat nonlinear. Cold pool and entrainment process exert positive and negative influences on convection intensity, respectively. On one hand, the cold-pool intensity and hence the positive effect on convection were similar between CNTL and DRY10 runs (see  $C$  and  $d\text{CAPE}_{0-1\text{km}}/dt$  in Table 3). On the other hand, drier air aloft in DRY10 produced stronger entrainment (negative effect) (see  $\varepsilon$  in Table 3), associated with the reduction in convection size (Fig. 5). Therefore, the convective updraft in DRY10 was more prone to the detrimental effect of dry-air entrainment than that in CNTL, and thus convection in DRY10 was weaker than that in CNTL. In other words, the nonlinear response of convection intensity to midlevel RH results from the compensating effects between cold-pool intensity and entrainment process. Note that DRY10 and CNTL experiments featured similar cold-pool intensity because the reduction in mixing ratio offset the enhancement in evaporative cooling in DRY10 (Table 3).

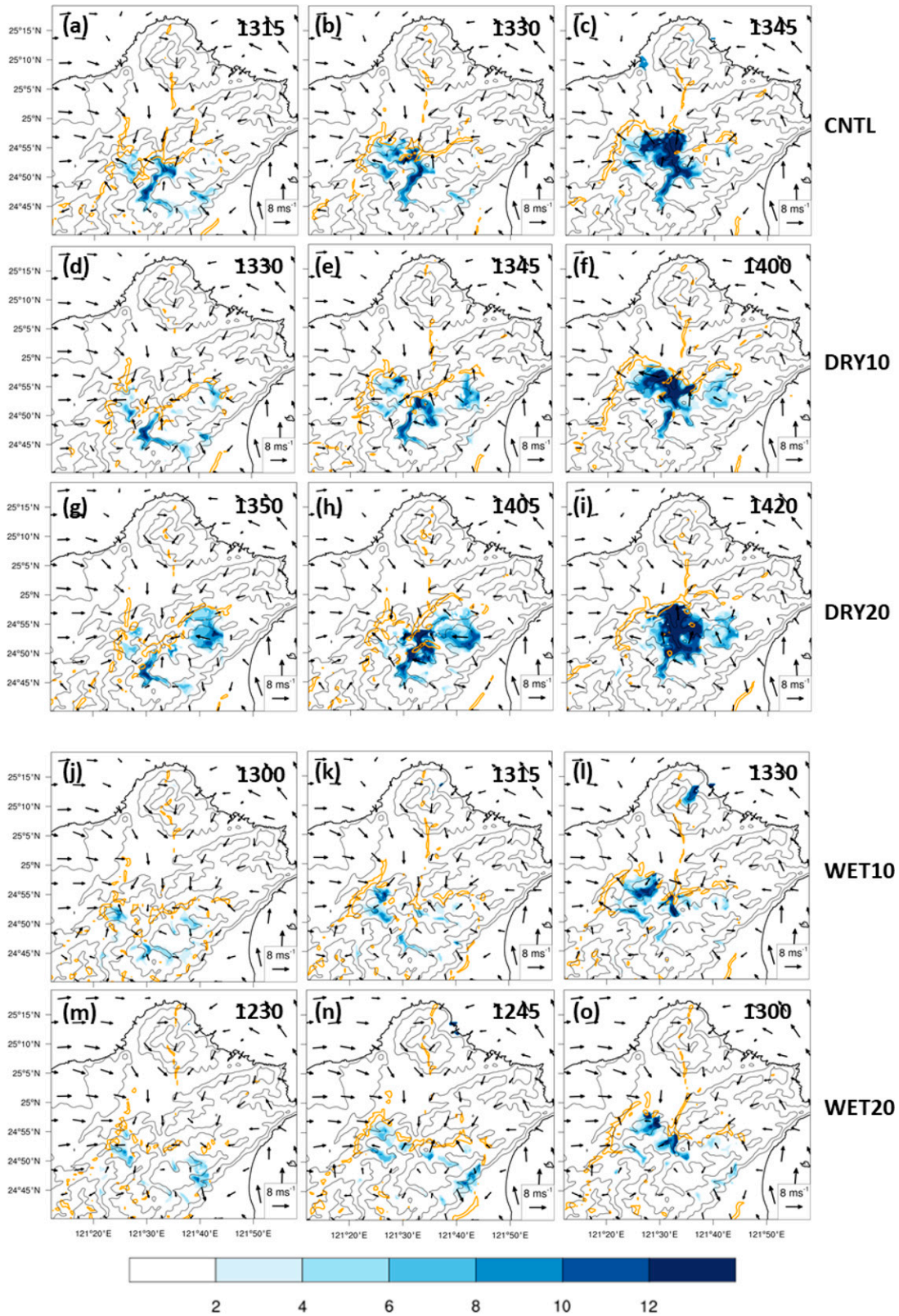


FIG. 11. Horizontal cross sections of cold-pool propagation speed (colored; unit:  $\text{m s}^{-1}$ ), 560-m vertical velocity (orange contours;  $2 \text{ m s}^{-1}$ ), and 10-m wind vectors from all experiments. Black line is for the terrain height contoured at 100, 300, 700, and 1300 m.

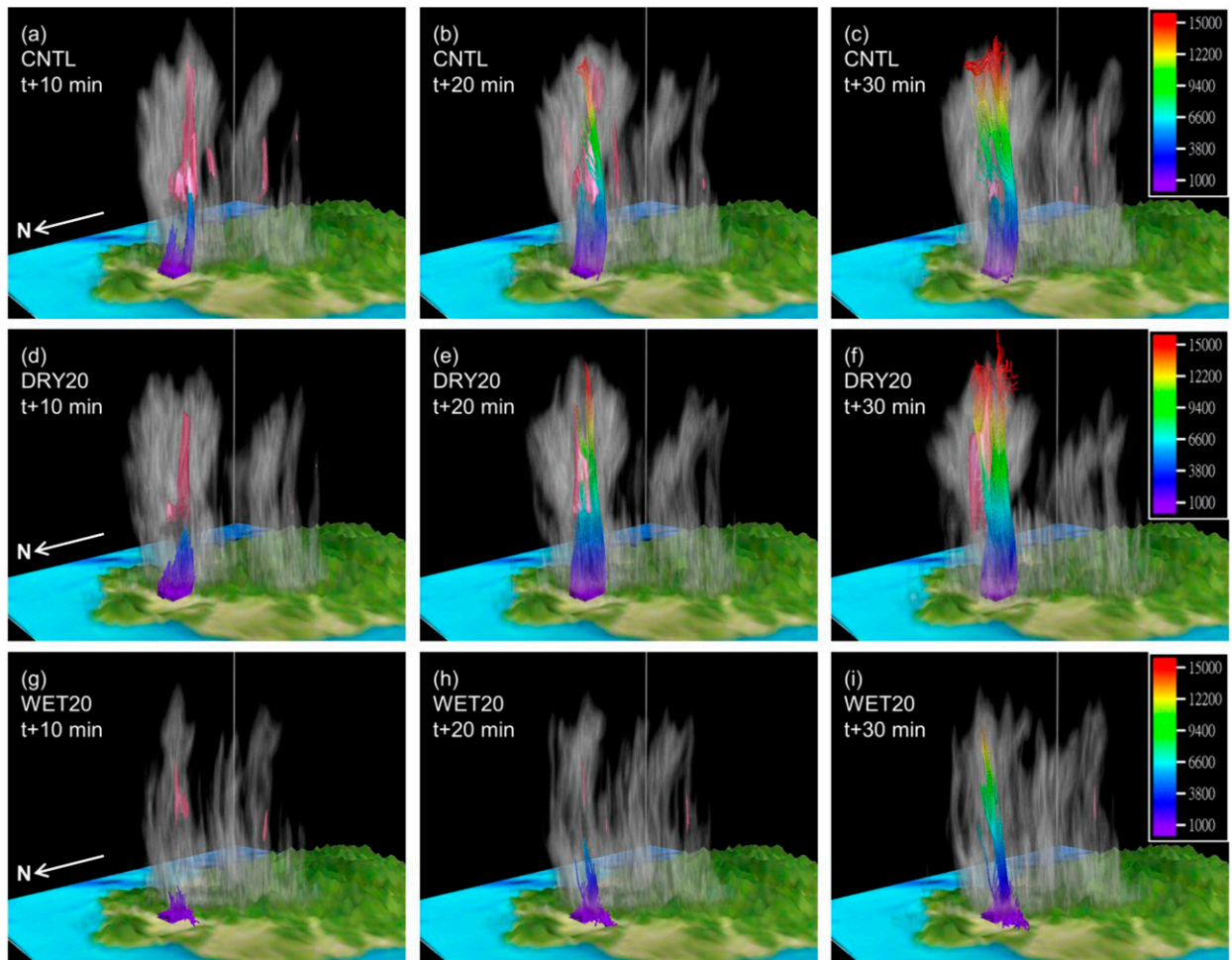


FIG. 12. (a)–(c) Three-dimensional perspective view of the graupel, cloud condensate (sum of cloud water and ice), and air parcel forward trajectories at (a)  $t + 10$  min, (b)  $t + 20$  min, and (c)  $t + 30$  min in the CNTL experiment. The initial time  $t$  of forward trajectories is at 1345 LST. The view is from the northwest. The isosurface of graupel (with mixing ratio =  $12 \text{ g kg}^{-1}$ ) is shown in raspberry color. Color scale along the trajectory indicates the height (unit: m MSL). Trajectories were initialized at every four model grid points within the rectangle at 400 and 600 m MSL for a total of 200 trajectories. (d)–(f) As in (a)–(c), but for trajectories starting at 1420 LST in DRY20 experiment. (g)–(i) As in (a)–(c), but for trajectories starting at 1300 LST in WET20 experiment.

#### d. Significance of midlevel dry air

We have examined the sensitivity of ATS intensity to midlevel moisture amount. However, there is a more fundamental problem to ask: Why and how was the ATS intensity sensitive to midlevel moisture? Cold-pool dynamics certainly played a critical role in convection development. As a result, it is natural to expect that a notable proportion of cold-pool parcels came from the middle levels. To verify this expectation, 60-min backward trajectories were calculated from 5-min outputs from the CNTL using the VAPOR software. A total of 200 air parcels were traced back from the cold pool within the central Taipei basin, with initial heights of 200 and 400 m MSL. Figure 16a displays the three-dimensional aerial view (from the top) of the 200 backward trajectories. By tracking the final position of these trajectories to the ending time ( $t - 60$  min), we find that 59% of cold-pool parcels were

above the TB one hour before, 18% were from the southern slope, 16% were from Keelung River valley, and 6% were from the west of TB (see Fig. 1d in MY20 for the geography of TB). Figure 16b shows the perspective view of 200 trajectories from the west of TB. It is clear that the air parcels from the southern slope were transported by the northward-propagating ATS, with the highest parcel height located at 6.5 km MSL. Trajectory ending-height histogram indicates that 37% of cold-pool parcels descended from 3 km MSL or higher (Fig. 17). These statistics support our hypothesis and explain why the storm intensity was sensitive to midlevel RH.

#### 5. Response of ATS to midlevel RH in the absence of Taiwan terrain

To investigate the effect of terrain on the response of convection to midlevel moisture content, we compare the NTER

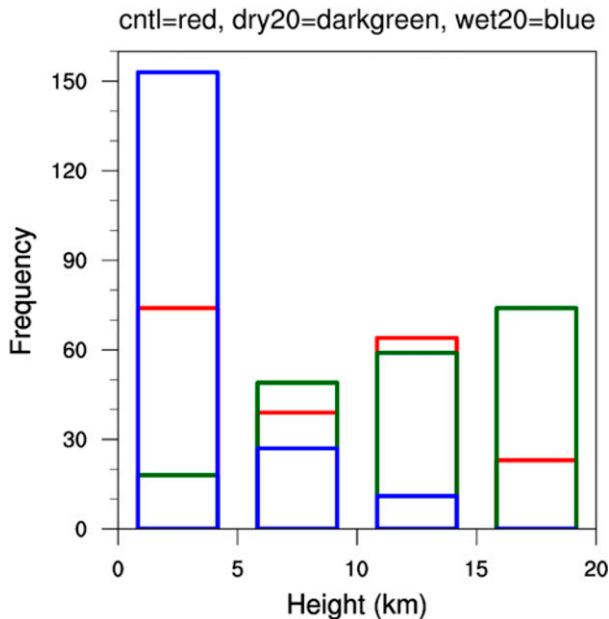


FIG. 13. Histogram of the final heights attained by the air parcels at  $t + 30$  min for the CNTL, DRY20, and WET20 experiments. For instance, the leftmost blue (red) bar indicates that 153 (74) parcels in WET20 (CNTL) experiment had final heights of less than 5 km MSL.

runs (CNTL\_NTER, DRY20\_NTER, WET20\_NTER) with full-terrain runs (CNTL, DRY20, WET20) in this section. The model configuration of NTER runs is the same as full-terrain runs except that the Taiwan terrain is totally removed. Due to the delayed convection initiation in NTER runs, we examined the evolution of ATS during 1400–1700 LST (Fig. 18). In full-terrain runs, scattered convection initiated at the mountain slope south of TB, then merged into the thunderstorm complex, and finally propagated northward to basin plain (Fig. 4). Moreover, enhanced low-level convergence produced by sea breeze (northerly) and thunderstorm outflow (southerly) played a vital role in convection development in full-terrain runs. In contrast, the sea breeze (northerly) converged with the large-scale southerly in NTER run (Fig. 18). The ATS convection initiated at the northeastern coast and then propagated southward in NTER runs, which is opposite to the full-terrain runs. The southward propagation of ATS in NTER runs is due to the absence of terrain and convective outflow (southerly) at the foothills south of TB. Moreover, NTER simulations had more scattered convection and much weaker convection intensity than those in full-terrain simulations. Regarding rainfall characteristics in the terrain-removal experiments, WET20\_NTER experiment had the most accumulated rainfall (Fig. 19), followed by CNTL\_NTER and DRY20\_NTER. Compared to the full-terrain runs, the accumulated rainfall in NTER runs decreased dramatically. It is worth noting that there were no TB-domain grid points with rainfall exceeding 40 mm in 30 min for NTER experiments (not shown). These results indicate that topography has a major impact on storm evolution and rainfall intensity.

For the TB-domain updraft mass flux of the NTER experiments, the updraft mass fluxes were stronger in WET20\_NTER and CNTL\_NTER experiments, with the contour of  $2 \times 10^9 \text{ kg s}^{-1}$  reaching about 15 km MSL (Figs. 20a,c). The updraft mass flux was weakest in DRY20\_NTER, with the contour of  $2 \times 10^9 \text{ kg s}^{-1}$  reaching only 6 km MSL (Fig. 20b). In addition, WET20\_NTER had the highest vertical velocity in the TB domain, followed by CNTL\_NTER and DRY20\_NTER (Fig. 21). These results are consistent with those in JM10. Note that the updraft mass flux in NTER runs was much weaker than that in full-terrain runs (cf. Figs. 7a,c,e and 20a,b,c). For example, the low-level maximum updraft mass flux in CNTL\_NTER run ( $\sim 6 \times 10^9 \text{ kg s}^{-1}$ ) was less than that in CNTL run ( $\sim 10 \times 10^9 \text{ kg s}^{-1}$ ) by 30%, and the upper-level maximum updraft mass flux in CNTL\_NTER ( $\sim 2 \times 10^9 \text{ kg s}^{-1}$ ) was less than CNTL ( $\sim 10 \times 10^9 \text{ kg s}^{-1}$ ) by 80%.

Before ATS convection dissipated (indicated by the dashed line in Fig. 20), DRY20\_NTER had the largest entrainment rate, followed by CNTL\_NTER and WET20\_NTER (Figs. 20d–f). By comparing NTER results with full-terrain results, we found two main differences. First, the entrainment rate in full-terrain runs was less than that in NTER runs (cf. Figs. 9a,c,e and 20d,e,f). Second, the entrainment rate decreased abruptly with the updraft mass flux in CNTL and DRY20 runs. However, due to the much smaller convection size, these phenomena did not occur in CNTL\_NTER and DRY20\_NTER runs.

These experiments have highlighted the most interesting possibility: The confined outflow associated with ATS within the TB was forced to converge with the moist sea breeze continuously, providing a favorable dynamic and thermodynamic environment for subsequent convection development. When more convective clouds are triggered at the collision boundary, the spacing among them is reduced and wider clouds are more frequently formed. As a result, the inner portion of updraft is protected by the nearby moist cloudy air, favoring the growth of the clouds into deep convection. In summary, the continuous low-level convergence within the basin plain supports cold-pool dynamics and impedes entrainment process. This “basin confinement effect” which results in continuous and enhanced low-level convergence within basin plain, may be crucial for short-duration rainfall extremes over complex terrain.

## 6. Discussion and summary

Expanding upon our previous research on the severe afternoon thunderstorm (ATS) system over the Taipei basin (TB) on 14 June 2015, we have investigated the influence of middle-level relative humidity (RH) on the sea-breeze thunderstorm over basin terrain in this study. The control simulation (CNTL) using the WRF Model with the horizontal grid size nested down to 500 m could reasonably capture the onset of the sea breeze, the merger of convective cells, and the evolution of the ATS system (Miao and Yang 2018; MY20). Four numerical sensitivity experiments that alternatively increased or decreased the midlevel RH by 10% and 20% were conducted. Results from the sensitivity experiments were then compared with those from the CNTL to understand the

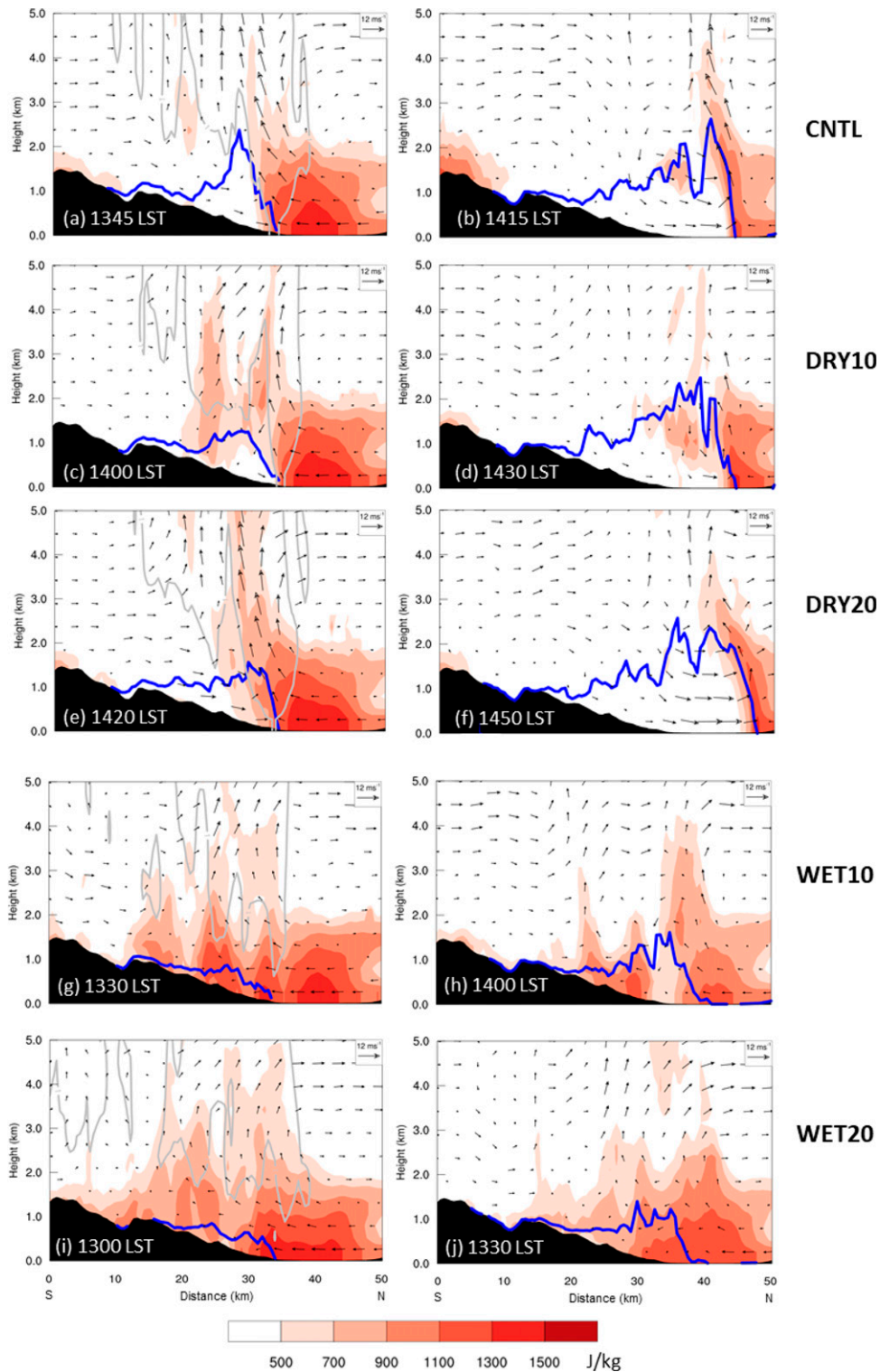


FIG. 14. Vertical sections of CAPE (unit:  $\text{J kg}^{-1}$ ; colored) for parcels lifted from each vertical level and cold-pool height (thick blue line) and vertical velocity ( $1 \text{ m s}^{-1}$ ; gray line). The vertical cross sections are along the N-S direction of the line shown in Fig. 4 (after the 10-km average in zonal direction). (a),(b) CNTL, (c),(d) DRY10, (e),(f) DRY20, (g),(h) WET10, and (i),(j) WET20 experiments. The time in LST is indicated at the lower-left corner of each panel. (a),(c),(e),(g),(i) Note that the contours of vertical velocity are only plotted at the time before convection development.

TABLE 3. TB-domain 1-h-averaged cold-pool variables [near-surface (35 m) buoyancy  $b$ , height  $h$ , propagation speed  $C$ ], the rate of change of 0–1-km CAPE  $dCAPE_{0-1km}/dt$ , rainwater mixing ratio  $q_r$ , evaporative cooling of rainwater  $cool_{evp}$ , and entrainment rate  $\varepsilon$  during the time period when the ATS system moved into the TB [i.e., from phase 2 (Figs. 4f–j) to phase 3 (Figs. 4k–o)]; “0–1-km CAPE” is defined as the vertically integrated CAPE from the surface to 1 km MSL.  $q_r$  and  $cool_{evp}$  are averaged over 0–6 km MSL.  $\varepsilon$  is averaged over 1.5–3 km MSL.

Variable	Expt				
	DRY20	DRY10	CNTL	WET10	WET20
$b$ ( $m\ s^{-2}$ )	−0.065	−0.059	−0.057	−0.044	−0.040
$h$ (m)	388	348	304	196	152
$C$ ( $m\ s^{-1}$ )	9.0	8.1	8.1	6.6	6.4
$dCAPE_{0-1km}/dt$ ( $J\ m^{-2}\ h^{-1}$ )	−0.33	−0.27	−0.26	−0.16	−0.05
$q_r$ ( $g\ kg^{-1}$ )	0.51	0.43	0.45	0.37	0.31
$cool_{evp}$ ( $K\ h^{-1}$ )	2.1	1.8	1.7	1.3	1.0
$\varepsilon$ ( $10^{-4}\ m^{-1}$ )	1.8	2.1	1.8	1.9	1.7

physical processes leading to the intense ATS when a midlevel layer of dry air occurred. In addition, three midlevel-RH experiments were performed with Taiwan terrain totally removed to examine how Taiwan terrain affected the response of ATS to the midlevel moisture content.

Sensitivity experiment results in section 4 indicated that dry air at middle levels would enhance evaporative cooling, thus producing strong downdrafts and cold pools. This is consistent with previous studies (e.g., Johns and Doswell 1992; Yang and Houze 1995; Gilmore and Wicker 1998). Although the response of convection to midlevel moisture content is somewhat nonlinear, this study focuses on the physical processes leading to heavy rainfall in a dry midlevel environment. Overall, the stronger cold pool of the ATS system in the CNTL

and DRY20 experiments would result in two indirect effects on convection:

- Stronger low-level convergence between colliding cold pools provides a favorable condition for convective cell merger (Tao and Simpson 1989; Carey and Rutledge 2000; Glenn and Krueger 2017; Miao and Yang 2018). The ATS system in CNTL and DRY20 experiments had larger convection size. Thus, the inner portion of convective updraft was shielded by the surrounding moist air and the bulk entrainment rate decreased significantly.
- Stronger low-level convergence between cold pool and sea breeze would lift most of moist parcels to upper levels, providing an abundant source of water vapor for the formation and growth of graupel particles. For example, 63% and 91% of parcels rose above the melting level (~5 km MSL) in the CNTL and DRY20 runs, respectively. On the contrary, only 24% of air parcels could reach above the melting level in the WET20 run. In other words, the ATS in CNTL and DRY20 experiments could consume the 0–1-km-integrated CAPE over the TB more effectively, producing stronger freezing and deposition warming at upper levels. Cold pool acts as a conveyor belt, transporting moist air parcels within the sea breeze to the level of free convection and releasing the conditional instability.

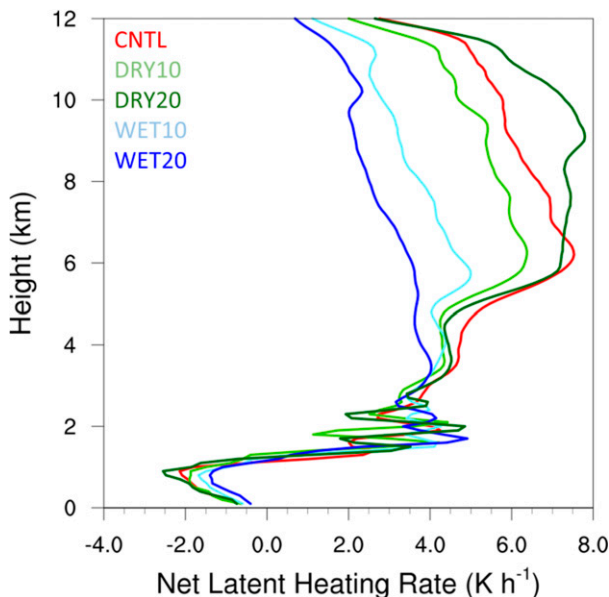


FIG. 15. Vertical profiles of TB domain 1-h-averaged net latent heating rate (unit:  $K\ h^{-1}$ ). Profiles are averaged over the TB domain during the time period when the simulated ATS system moved into the TB.

Because of the above-mentioned indirect effects of dry air, CNTL and DRY20 experiments had stronger cold pools, more intense convection, stronger updrafts, more graupel particles, stronger net latent heating above the melting level, and much larger areas of the potential flooding region [ $>40\ mm\ (30\ min)^{-1}$ ]. On the other hand, a moister midlevel layer (i.e., WET10 and WET20 experiments) would induce less evaporative cooling and shallower cold pool, producing weaker convection, resulting in a much smaller area of the potential flooding region. Figure 22 is the schematic diagram illustrating the response of ATS to midlevel RH for this case over the Taipei basin on 14 June 2015, under the environment with drier and wetter midlevel conditions. It should be noted that these results can only support the conclusion that drier air leads to stronger convection in this specific scenario of topography and sea breeze. Schumacher and Peters (2017) indicated

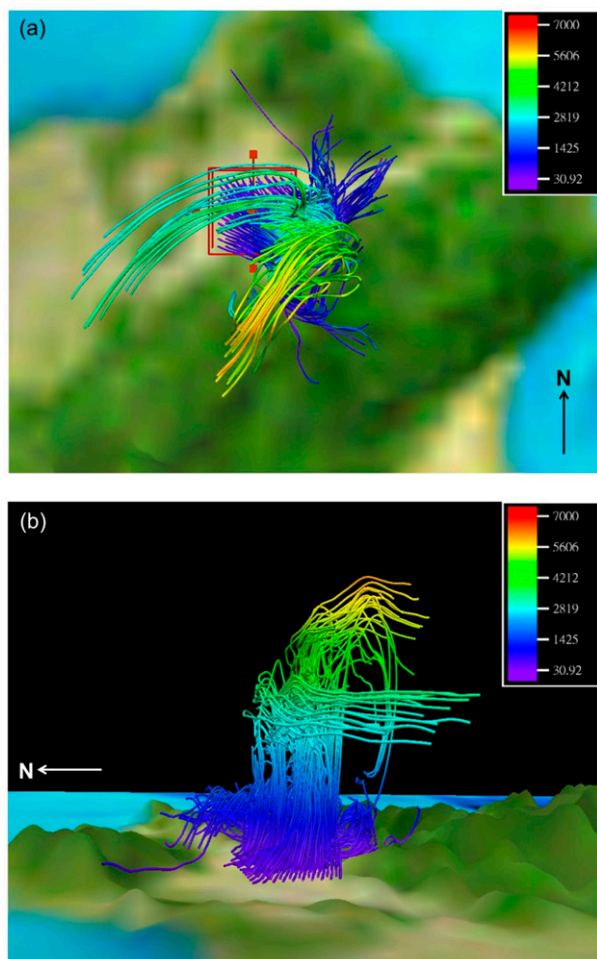


FIG. 16. Three-dimensional view of the 60-min air parcel backward trajectories in the CNTL experiment. The view is from the (a) top and (b) west. The starting (ending) time  $t$  ( $t - 60$  min) of backward trajectories is 1415 (1315) LST. Color scale along the trajectory indicates the height (unit: m MSL). Trajectories were initialized at every four model grid points within the square [the red box in (a)] at 200 and 400 m MSL for a total of 200 trajectories.

that the convective rainfall was highly sensitive to the minor variations in low-level moisture. Our study suggests that the occurrence of short-duration intense rainfall produced by the sea-breeze thunderstorm over basin terrain may increase remarkably with the decreased midlevel moisture. This issue is rarely discussed in previous studies.

Note that convection in DRY10 was weaker than that in CNTL, suggesting a nonlinear response of convection intensity to midlevel RH. Except for the indirect effects of midlevel dry air on convection, the entrainment process (direct effect) is detrimental to convection. In other words, cold pool and entrainment process exert positive and negative influences on convection intensity, respectively. On one hand, the cold-pool intensity and hence the positive effect on convection were similar between the CNTL and DRY10 runs. On the other hand, drier air aloft in DRY10 produced

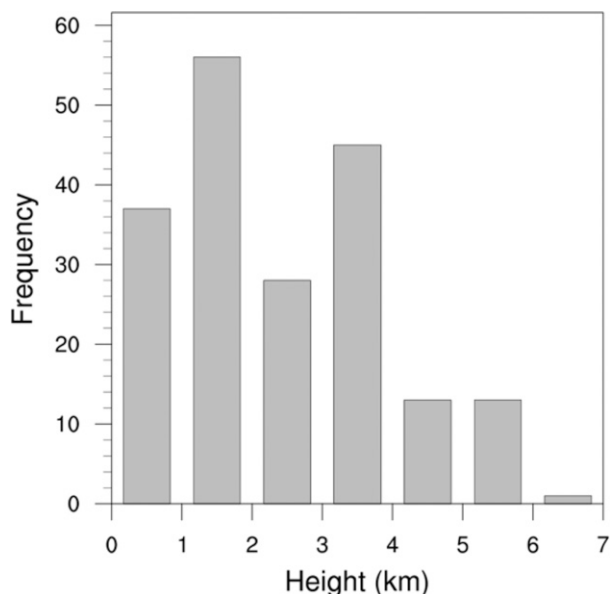


FIG. 17. Histogram of the heights of backward trajectories at the ending time of  $t - 60$  min.

stronger entrainment (negative effect), associated with the reduction in convection size. Therefore, the convective updraft in DRY10 was more prone to the detrimental effect of dry-air entrainment than that in CNTL, and thus convection in DRY10 is weaker. To put it succinctly, the nonlinear response of convection intensity to midlevel RH results from the compensating effects between cold-pool intensity and entrainment process.

JM10 investigated the sensitivity of squall lines and supercells to the midlevel dry air. They found that dry air aloft reduced total condensation, total rainfall, and total mass of each condensate species. The updraft and downdraft mass fluxes were also reduced, except in high-CAPE simulation. Moreover, the cold-pool intensity was either unchanged or reduced because the increased evaporative cooling could not offset the decrease of hydrometeor mass. Their results do not contradict our current study on ATSS. First of all, in this extreme ATS case, solar heating and abundant moisture brought by sea breeze increased the CAPE over the TB, providing large conditional instability for the intensification of the thunderstorm convection (MY20). This high-CAPE environment ( $\sim 3500 \text{ J kg}^{-1}$ ) produced intense convective storms, which were able to resist the detrimental effect from ambient dry air. The estimation of bulk entrainment rate provides evidence that the entrainment rate could be reduced by stronger cold pool and the widening of moist convection area, consistent with previous studies (e.g., Kuang and Bretherton 2006; Khairoutdinov and Randall 2006; Khairoutdinov et al. 2009; Kurowski et al. 2018). Interestingly, using the buoyancy-sorting model (Raymond and Blyth 1986; Kain and Fritsch 1990), JM10 also indicated that the convection in the high-CAPE environment was capable of withstanding the deleterious effect of dry air aloft.

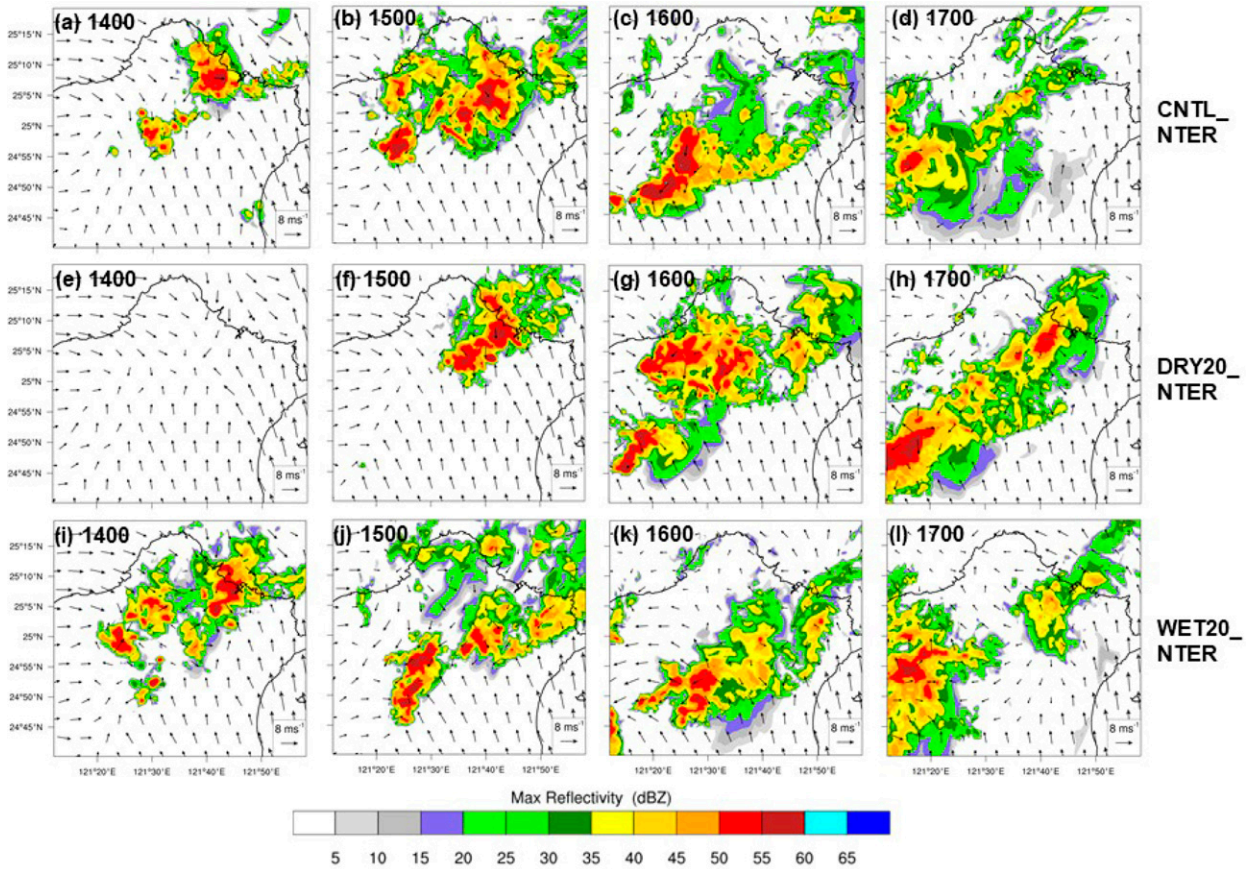


FIG. 18. As in Fig. 4, but for (a)–(d) CNTL\_NTER, (e)–(h) DRY20\_NTER, and (i)–(l) WET20\_NTER experiments during 1400–1700 LST.

Second, this study examines the ATS system over complex basin terrain, which is different from the convective systems over flat terrain discussed in JM10. The terrain sensitivity experiments in section 5 have highlighted the most interesting possibility: The confined outflow associated with ATS within the TB is forced to converge with the moist sea breeze

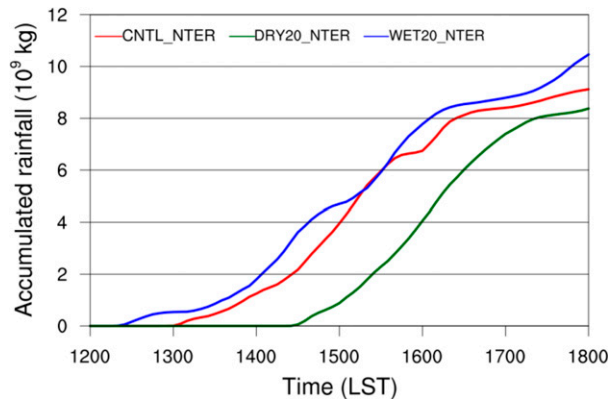


FIG. 19. As in Fig. 6a, but for CNTL\_NTER, DRY20\_NTER, and WET20\_NTER experiments during 1200–1800 LST. Note that the y axis is up to  $12 \times 10^9$  kg.

continuously, providing a favorable dynamic and thermodynamic environment for subsequent convection development. When more convective clouds are triggered at the collision boundary, the spacing among them is reduced and wider clouds are more frequently formed. As a result, the inner portion of updraft is protected by the nearby moist cloudy air, favoring the growth of the clouds into deep convection. To put it succinctly, the continuous low-level convergence within the basin plain supports cold-pool dynamics and impedes entrainment process. This “basin confinement effect” which modulates the response of convection to midlevel RH may be crucial for short-duration rainfall extremes over complex terrain. This “basin confinement effect” is a unique feature which is rarely discussed in previous studies on ATS systems over basin terrain.

Previous ATS occurrence checklist (Lin et al. 2012; C16) indicated that midlevel moist air was favorable for thunderstorm development in a “weak synoptic environment,” but the checklist did not perform well on this extreme rainfall case which resulted in urban-scale flooding. There are two possible reasons. First, the composite analysis would miss the extreme cases (i.e., statistics outliers). Second, when the western North Pacific subtropical high covers northern Taiwan, the low and middle troposphere is relatively dry, inhibiting

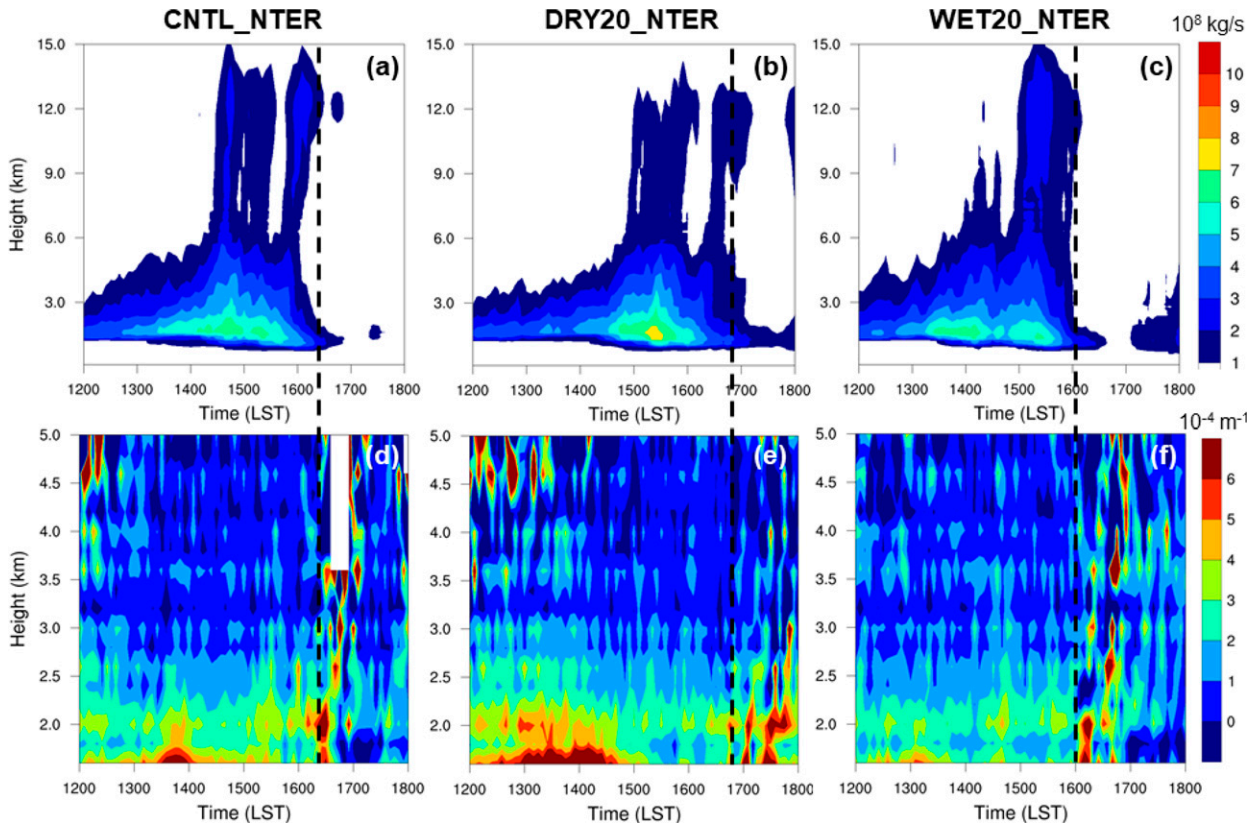


FIG. 20. (a)–(c) As in Fig. 7, but for (a) CNTL\_NTER, (b) DRY20\_NTER, and (c) WET20\_NTER experiments during 1200–1800 LST. (d)–(f) As in Fig. 9, but for (d) CNTL\_NTER, (e) DRY20\_NTER, and (f) WET20\_NTER experiments during 1200–1800 LST. Dashed line indicates the last time when the updraft mass flux is greater than  $3 \times 10^9 \text{ kg s}^{-1}$ .

convection development. Note that midlevel dryness is usually associated with low-level dryness in this scenario. However, northern Taiwan was in the vicinity of the western North Pacific subtropical high for this case, with the deep dry air above moist air. It is suggested that the midlevel (700–500 hPa) mean RH and DCAPE may be critical predictors in severe ATS

forecast and warrant further investigation. In addition, the location of western North Pacific subtropical high needs to be reexamined to better define the condition for “weak synoptic environment.”

Even though this study can provide valuable insights into the thunderstorm dynamics under the influence of midlevel dry air and complex terrain, it has some limitations. First, conclusions obtained in this study are mainly based on numerical simulations with some model deficiencies, physics uncertainties, and numerical errors, so we should keep these caveats in mind. Second, the nonlinear response of convection intensity to midlevel RH may limit the generalization of the results to other thunderstorm events. More case studies are required to generalize the findings from this particular afternoon thunderstorm case to other thunderstorm events in the future. Furthermore, the midlevel moisture sensitivity experiments in this study only address limited aspects of the predictability of the ATS rainfall over the TB. Further works are still needed to examine the sensitivity of ATS rainfall to a broader range of environmental conditions. For example, the large-scale wind direction (Wang and Sobel 2017) and low-level thermodynamic environment (Chen et al. 2017) could also significantly impact the ATSS and their accumulated rainfall.

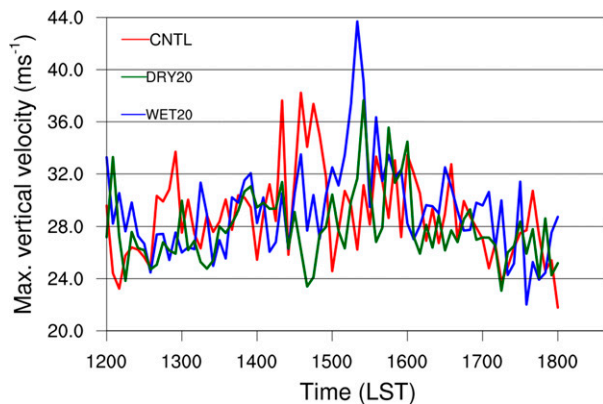


FIG. 21. TB domain-maximum vertical velocity (unit:  $\text{m s}^{-1}$ ) during 1200–1800 LST from all terrain-removal experiments.

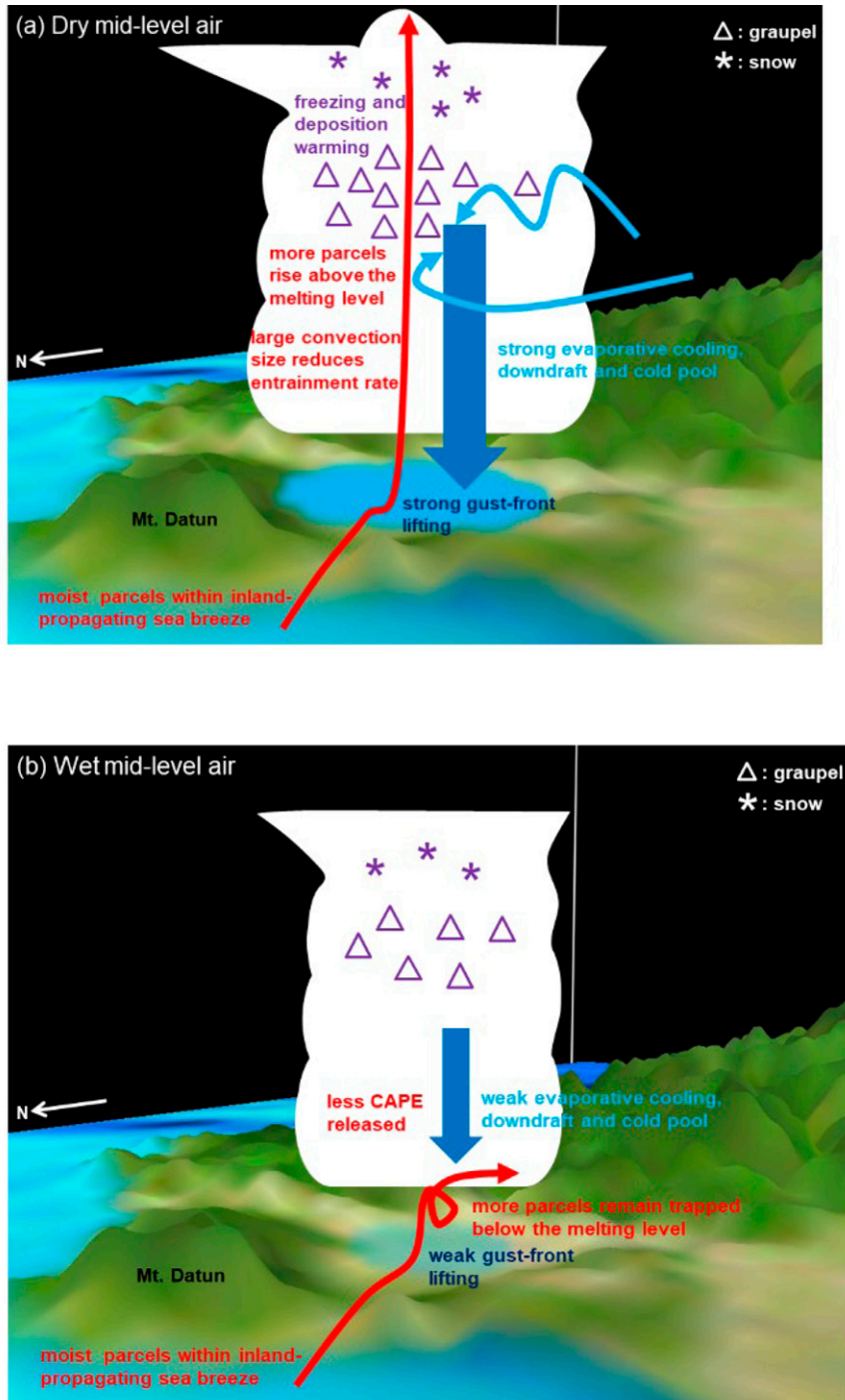


FIG. 22. Schematic diagram based on the sensitivity experiment results: (a) the control simulation where the environmental middle levels are dry (CNTL) and (b) the experiment where the environmental middle levels are relatively wet (WET20).

*Acknowledgments.* Constructive comments by the editor and the reviewers on our manuscript are highly appreciated. We thank the Central Weather Bureau in Taiwan for providing the observation data. This work was supported by the Ministry of Science and Technology in Taiwan under

Grants MOST 108-2625-M-052-003, MOST 108-2111-M-002-011-MY2, and MOST 110-2111-M-002-014.

*Data availability statement.* The HYSPLIT transport and dispersion model and READY website (<https://www.ready.noaa.gov>)

are provided by the NOAA Air Resources Laboratory (ARL). The Visualization and Analysis Platform for Atmospheric, Oceanic and solar Research (VAPOR) software (<https://vapor.ucar.edu>) used in this study is provided by NCAR. The WRF Model used in this study is available online at [github.com/NCAR/WRFV3](https://github.com/NCAR/WRFV3). Numerical experiments outputs are available from the corresponding author (mingjen@as.ntu.edu.tw) upon reasonable request.

## REFERENCES

- Brown, R. G., and C. Zhang, 1997: Variability of midtropospheric moisture and its effects on cloud-top height distribution during TOGA COARE. *J. Atmos. Sci.*, **54**, 2760–2774, [https://doi.org/10.1175/1520-0469\(1997\)054<2760:VOMMAI>2.0.CO;2](https://doi.org/10.1175/1520-0469(1997)054<2760:VOMMAI>2.0.CO;2).
- Browning, K. A., and F. H. Ludlum, 1962: Airflow in convective storms. *Quart. J. Roy. Meteor. Soc.*, **88**, 117–135, <https://doi.org/10.1002/qj.49708837602>.
- Bryan, G. H., and M. D. Parker, 2010: Observations of a squall line and its near environment using high-frequency rawinsonde launches during VORTEX2. *Mon. Wea. Rev.*, **138**, 4076–4097, <https://doi.org/10.1175/2010MWR3359.1>.
- Carey, L. D., and S. A. Rutledge, 2000: The relationship between precipitation and lightning in tropical island convection: A C-band polarimetric radar study. *Mon. Wea. Rev.*, **128**, 2687–2710, [https://doi.org/10.1175/1520-0493\(2000\)128<2687:TRBPAL>2.0.CO;2](https://doi.org/10.1175/1520-0493(2000)128<2687:TRBPAL>2.0.CO;2).
- Chen, C., and C. Liu, 2014: The definition of urban stormwater tolerance threshold and its conceptual estimation: An example from Taiwan. *Nat. Hazards*, **73**, 173–190, <https://doi.org/10.1007/s11069-013-0645-7>.
- Chen, G. T.-J., H.-C. Chou, T. C. Chang, and C. S. Liu, 2001: Frontal and non-frontal convection over northern Taiwan in mei-yu season (in Chinese with English abstract). *Atmos. Sci.*, **29**, 37–52.
- Chen, T.-C., S.-Y. Wang, and M.-C. Yen, 2007: Enhancement of afternoon thunderstorm activity by urbanization in a valley: Taipei. *J. Appl. Meteor. Climatol.*, **46**, 1324–1340, <https://doi.org/10.1175/JAM2526.1>.
- , J. Tsay, and E. S. Takle, 2016: A forecast advisory for afternoon thunderstorm occurrence in the Taipei basin during summer developed from diagnostic analysis. *Wea. Forecasting*, **31**, 531–552, <https://doi.org/10.1175/WAF-D-15-0082.1>.
- Chen, X., F. Zhang, and K. Zhao, 2017: Influence of monsoonal wind speed and moisture content on intensity and diurnal variations of the mei-yu season coastal rainfall over South China. *J. Atmos. Sci.*, **74**, 2835–2856, <https://doi.org/10.1175/JAS-D-17-0081.1>.
- Clyne, J., and M. Rast, 2005: A prototype discovery environment for analyzing and visualizing terascale turbulent fluid flow simulations. *Proc. SPIE*, **5669**, 284–294, <https://doi.org/10.1117/12.586032>.
- , P. Mininni, A. Norton, and M. Rast, 2007: Interactive desktop analysis of high-resolution simulations: Application to turbulent plume dynamics and current sheet formation. *New J. Phys.*, **9**, 301, <https://doi.org/10.1088/1367-2630/9/8/301>.
- Dee, D. P., and Coauthors, 2011: The ERA-Interim reanalysis: Configuration and performance of the data assimilation system. *Quart. J. Roy. Meteor. Soc.*, **137**, 553–597, <https://doi.org/10.1002/qj.828>.
- Dudhia, J., 1989: Numerical study of convection observed during the Winter Monsoon Experiment using a mesoscale two-dimensional model. *J. Atmos. Sci.*, **46**, 3077–3107, [https://doi.org/10.1175/1520-0469\(1989\)046<3077:NSOCOD>2.0.CO;2](https://doi.org/10.1175/1520-0469(1989)046<3077:NSOCOD>2.0.CO;2).
- Emanuel, K. A., 1994: *Atmospheric Convection*. Oxford University Press, 580 pp.
- Fawbush, E. J., and R. C. Miller, 1954: The types of airmasses in which North American tornadoes form. *Bull. Amer. Meteor. Soc.*, **35**, 154–165, <https://doi.org/10.1175/1520-0477-35.4.154>.
- Feng, Z., S. Hagos, A. K. Rowe, C. D. Burleyson, M. N. Martini, and S. P. de Szoeke, 2015: Mechanisms of convective cloud organization by cold pools over tropical warm ocean during the AMIE/DYNAMO field campaign. *J. Adv. Model. Earth Syst.*, **7**, 357–381, <https://doi.org/10.1002/2014MS000384>.
- Foster, D. S., 1958: Thunderstorm gusts compared with computed downdraft speeds. *Mon. Wea. Rev.*, **86**, 91–94, [https://doi.org/10.1175/1520-0493\(1958\)086<0091:TGCWCD>2.0.CO;2](https://doi.org/10.1175/1520-0493(1958)086<0091:TGCWCD>2.0.CO;2).
- Gilmore, M. S., and L. J. Wicker, 1998: The influence of midtropospheric dryness on supercell morphology and evolution. *Mon. Wea. Rev.*, **126**, 943–958, [https://doi.org/10.1175/1520-0493\(1998\)126<0943:TJOMDO>2.0.CO;2](https://doi.org/10.1175/1520-0493(1998)126<0943:TJOMDO>2.0.CO;2).
- Glenn, I. B., and S. K. Krueger, 2017: Connections matter: Updraft merging in organized tropical deep convection. *Geophys. Res. Lett.*, **44**, 7087–7094, <https://doi.org/10.1002/2017GL074162>.
- Hohenegger, C., and C. S. Bretherton, 2011: Simulating deep convection with a shallow convection scheme. *Atmos. Chem. Phys.*, **11**, 10389–10406, <https://doi.org/10.5194/acp-11-10389-2011>.
- Hong, S.-Y., and H.-L. Pan, 1996: Nonlocal boundary layer vertical diffusion in a medium-range forecast model. *Mon. Wea. Rev.*, **124**, 2322–2339, [https://doi.org/10.1175/1520-0493\(1996\)124<2322:NBLVDI>2.0.CO;2](https://doi.org/10.1175/1520-0493(1996)124<2322:NBLVDI>2.0.CO;2).
- James, R. P., and P. M. Markowski, 2010: A numerical investigation of the effects of dry air aloft on deep convection. *Mon. Wea. Rev.*, **138**, 140–161, <https://doi.org/10.1175/2009MWR3018.1>.
- Johns, R. H., and C. A. Doswell III, 1992: Severe local storms forecasting. *Wea. Forecasting*, **7**, 588–612, [https://doi.org/10.1175/1520-0434\(1992\)007<0588:SLSF>2.0.CO;2](https://doi.org/10.1175/1520-0434(1992)007<0588:SLSF>2.0.CO;2).
- Johnson, R. H., and J. F. Breach, 1991: Diagnosed characteristics of precipitation systems over Taiwan during the May–June 1987 TAMEX. *Mon. Wea. Rev.*, **119**, 2540–2557, [https://doi.org/10.1175/1520-0493\(1991\)119<2540:DCOPSO>2.0.CO;2](https://doi.org/10.1175/1520-0493(1991)119<2540:DCOPSO>2.0.CO;2).
- Jou, B. J. D., 1994: Mountain-originated mesoscale precipitation system in northern Taiwan: A case study of 21 June 1991. *Terr. Atmos. Ocean. Sci.*, **5**, 169–197, [https://doi.org/10.3319/TAO.1994.5.2.169\(TAMEX\)](https://doi.org/10.3319/TAO.1994.5.2.169(TAMEX)).
- , Y.-C. Kao, R.-G. R. Hsiu, C.-J. U. Jung, J. R. Lee, and H. C. Kuo, 2016: Observational characteristics and forecast challenge of Taipei flash flood afternoon thunderstorm: Case study of 14 June 2015 (in Chinese with English abstract). *Atmos. Sci.*, **44**, 57–82.
- Kain, J. S., and J. M. Fritsch, 1990: A one-dimensional entraining/detraining plume model and its application in convective parameterization. *J. Atmos. Sci.*, **47**, 2784–2802, [https://doi.org/10.1175/1520-0469\(1990\)047<2784:AODEPM>2.0.CO;2](https://doi.org/10.1175/1520-0469(1990)047<2784:AODEPM>2.0.CO;2).
- , and —, 1993: Convective parameterization for mesoscale models: The Kain-Fritsch scheme. *The Representation of Cumulus Convection in Numerical Models*, Meteor. Monogr., No. 46, Amer. Meteor. Soc., 165–177.
- Khairoutdinov, M. F., and D. Randall, 2006: High-resolution simulation of shallow to deep convection transition over land. *J. Atmos. Sci.*, **63**, 3421–3436, <https://doi.org/10.1175/JAS3810.1>.
- , S. K. Krueger, C.-H. Moeng, P. A. Bogenschutz, and D. Randall, 2009: Large-eddy simulation of maritime deep

- tropical convection. *J. Adv. Model. Earth Syst.*, **1** (4), <https://doi.org/10.3894/JAMES.2009.1.15>.
- Kuang, Z., and C. S. Bretherton, 2006: A mass-flux scheme view of a high-resolution simulation of a transition from shallow to deep cumulus convection. *J. Atmos. Sci.*, **63**, 1895–1909, <https://doi.org/10.1175/JAS3723.1>.
- Kurowski, M. J., K. Suseelj, W. W. Grabowski, and J. Teixeira, 2018: Shallow-to-deep transition of continental moist convection: Cold pools, surface fluxes, and mesoscale organization. *J. Atmos. Sci.*, **75**, 4071–4090, <https://doi.org/10.1175/JAS-D-18-0031.1>.
- Lim, K.-S. S., and S.-Y. Hong, 2010: Development of an effective double-moment cloud microphysics scheme with prognostic cloud condensation nuclei (CCN) for weather and climate models. *Mon. Wea. Rev.*, **138**, 1587–1612, <https://doi.org/10.1175/2009MWR2968.1>.
- Lin, P.-F., P.-L. Chang, B. J.-D. Jou, J. W. Wilson, and R. D. Roberts, 2011: Warm season afternoon thunderstorm characteristics under weak synoptic-scale forcing over Taiwan Island. *Wea. Forecasting*, **26**, 44–60, <https://doi.org/10.1175/2010WAF2222386.1>.
- , —, —, and —, 2012: Objective prediction of warm season afternoon thunderstorms in northern Taiwan using a fuzzy logic approach. *Wea. Forecasting*, **27**, 1178–1197, <https://doi.org/10.1175/WAF-D-11-00105.1>.
- Miao, J.-E., and M.-J. Yang, 2018: Cell merger and heavy rainfall of the severe afternoon thunderstorm event at Taipei on 14 June 2015 (in Chinese with English abstract). *Atmos. Sci.*, **46**, 427–453.
- , and —, 2020: A modeling study of the severe afternoon thunderstorm event at Taipei on 14 June 2015: The roles of sea breeze, microphysics, and terrain. *J. Meteor. Soc. Japan*, **98**, 129–152, <https://doi.org/10.2151/jmsj.2020-008>.
- Mlawer, E. J., S. J. Taubman, P. D. Brown, M. J. Iacono, and S. A. Clough, 1997: Radiative transfer for inhomogeneous atmospheres: RRTM, a validated correlated-k model for the longwave. *J. Geophys. Res.*, **102**, 16 663–16 682, <https://doi.org/10.1029/97JD00237>.
- Moseley, C., C. Hohenegger, P. Berg, and J. O. Haerter, 2016: Intensification of convective extremes driven by cloud–cloud interaction. *Nat. Geosci.*, **9**, 748–752, <https://doi.org/10.1038/ngeo2789>.
- Parsons, D. B., J.-L. Redelsperger, and K. Yoneyama, 2000: The evolution of the tropical western Pacific atmosphere–ocean system following the arrival of a dry intrusion. *Quart. J. Roy. Meteor. Soc.*, **126**, 517–548, <https://doi.org/10.1002/qj.49712656307>.
- Raymond, D. J., and A. M. Blyth, 1986: A stochastic mixing model for nonprecipitating cumulus clouds. *J. Atmos. Sci.*, **43**, 2708–2718, [https://doi.org/10.1175/1520-0469\(1986\)043<2708:ASMMFN>2.0.CO;2](https://doi.org/10.1175/1520-0469(1986)043<2708:ASMMFN>2.0.CO;2).
- Richardson, Y. P., K. K. Droegemeier, and R. P. Davies-Jones, 2007: The influence of horizontal environmental variability on numerically simulated convective storms. Part I: Variations in vertical shear. *Mon. Wea. Rev.*, **135**, 3429–3455, <https://doi.org/10.1175/MWR3463.1>.
- Rolph, G., A. Stein, and B. Stunder, 2017: Real-time Environmental Applications and Display System: READY. *Environ. Modell. Software*, **95**, 210–228, <https://doi.org/10.1016/j.envsoft.2017.06.025>.
- Rotunno, R., J. B. Klemp, and M. L. Weisman, 1988: A theory for strong, long-lived squall line. *J. Atmos. Sci.*, **45**, 463–485, [https://doi.org/10.1175/1520-0469\(1988\)045<0463:ATFSL>2.0.CO;2](https://doi.org/10.1175/1520-0469(1988)045<0463:ATFSL>2.0.CO;2).
- Schumacher, R. S., and J. M. Peters, 2017: Near-surface thermodynamic sensitivities in simulated extreme-rain-producing mesoscale convective systems. *Mon. Wea. Rev.*, **145**, 2177–2200, <https://doi.org/10.1175/MWR-D-16-0255.1>.
- Skamarock, W. C., and Coauthors, 2008: A description of the Advanced Research WRF version 3. NCAR Tech. Note NCAR/TN-475+STR, 113 pp., <https://doi.org/10.5065/D68S4MVH>.
- Stein, A. F., R. R. Draxler, G. D. Rolph, B. J. B. Stunder, M. D. Cohen, and F. Ngan, 2015: NOAA’s HYSPLIT atmospheric transport and dispersion modeling system. *Bull. Amer. Meteor. Soc.*, **96**, 2059–2077, <https://doi.org/10.1175/BAMS-D-14-00110.1>.
- Takemi, T., O. Hirayama, and C. Liu, 2004: Factors responsible for the vertical development of tropical oceanic cumulus convection. *Geophys. Res. Lett.*, **31**, L11109, <https://doi.org/10.1029/2004GL020225>.
- Tao, W.-K., and J. Simpson, 1989: A further study of cumulus interactions and mergers: Three-dimensional simulations with trajectory analyses. *J. Atmos. Sci.*, **46**, 2974–3004, [https://doi.org/10.1175/1520-0469\(1989\)046<2974:AFSOCI>2.0.CO;2](https://doi.org/10.1175/1520-0469(1989)046<2974:AFSOCI>2.0.CO;2).
- Tompkins, A. M., 2001: Organization of tropical convection in low vertical wind shears: The role of cold pools. *J. Atmos. Sci.*, **58**, 1650–1672, [https://doi.org/10.1175/1520-0469\(2001\)058<1650:OOTCIL>2.0.CO;2](https://doi.org/10.1175/1520-0469(2001)058<1650:OOTCIL>2.0.CO;2).
- Wang, S., and A. H. Sobel, 2017: Factors controlling rain on small tropical islands: Diurnal cycle, large-scale wind speed, and topography. *J. Atmos. Sci.*, **74**, 3515–3532, <https://doi.org/10.1175/JAS-D-16-0344.1>.
- Yang, M.-J., and R. A. Houze Jr., 1995: Sensitivity of squall-line rear inflow to ice microphysics and environmental humidity. *Mon. Wea. Rev.*, **123**, 3175–3193, [https://doi.org/10.1175/1520-0493\(1995\)123<3175:SOSLRI>2.0.CO;2](https://doi.org/10.1175/1520-0493(1995)123<3175:SOSLRI>2.0.CO;2).